2007

Investigation of superficial dose from a static TomoTherapy beam

Koren Suzette Smith
Louisiana State University and Agricultural and Mechanical College

Recommended Citation

Smith, Koren Suzette, "Investigation of superficial dose from a static TomoTherapy beam" (2007). *LSU Master's Theses*. 1493.
https://digitalcommons.lsu.edu/gradschool_theses/1493

INVESTIGATION OF SUPERFICIAL DOSE FROM A STATIC TOMOTHERAPY BEAM

A THESIS

Submitted to the Graduate Faculty of the
Louisiana State University and
Agricultural and Mechanical College
in partial fulfillment of the
requirements for the Degree of
Master of Science

in

The Department of Physics and Astronomy

by
Koren Suzette Smith
B.S. Louisiana State University, 2004
May 2007

Acknowledgements

I would like to thank the members of my advisory committee: I thank Dr. John Gibbons for his guidance and encouragement throughout this research project and my time in graduate school; I thank Dr. Kenneth Hogstrom for his ideas and oversight; I thank Dr. Bruce Gerbi for sharing his knowledge and experience on the subject of this research; I thank Dr. Mette Gaarde for providing departmental oversight and I thank Dr. Greg Henkelmann for his clinical perspective. I would also like to thank Dr. Dennis Cheek and Dr. Isaac Rosen for their input and assistance.

I thank my parents, Ted and Mary, for their endless support and encouragement and I thank my sisters, Dara, Katie, and Valerie, for being incredible role models of intelligence and ambition. I thank my classmates, Justin, Allen, Scott and Will, for providing much needed distraction and entertainment during the work day.

Lastly, I would like to thank MBPCC for the use of their TomoTherapy unit, their TomoTherapy treatment planning system and other equipment.

Table of Contents

List of Tables

List of Figures

Abstract

Purpose: The TomoTherapy planning system is capable of creating treatment plans that deliver a homogeneous dose to superficial targets. It is essential that the planning system accurately predicts dose to the surface and superficial depths from beams directed at every angle in the axial plane. This work concentrates on measuring and modeling the dose from a static TomoTherapy beam at normal and oblique incidence. It was hypothesized that superficial doses measured from a static TomoTherapy beam agree with doses calculated by the TomoTherapy planning system to within 5% of the maximum dose for angles of incidence from 0˚-83˚.

Methods: Doses were measured with a parallel-plate chamber and TLDs at depths ≤ 2cm for 40x2.5cm^2 and 40x5cm^2 static TomoTherapy beams for multiple SSDs for incident angles of 0˚-83˚. The measurements made with TLDs were compared to those made with the parallel-plate chamber to verify the measured dose. The TomoTherapy treatment planning system was used to calculate doses from single, static beams incident on a flat phantom so that measured and calculated doses could be compared.

Results: Surface dose increased from 16.7%-18.9% as the SSD decreased from 85 to 55cm for the 40x5cm^2 field and from 12.7%-14.9% for the 40x2.5cm^2 field. The surface dose increased from 16.8%-44.2% as the angle of incidence increased from 0˚-83˚ for the 40x5cm^2 field and from 12.8%-42.6% for the 40x2.5cm^2 field. For all measurement conditions, the planning system under predicted the dose at the surface by more than 5%. For the following measurement conditions and depths, the planning system also under predicted the dose by more the 5%: 85 and 70cm SCD at a depth of 0.1cm, 55cm SCD at a depth of 0.2cm, and 30˚ and 45˚ at a depth of 0.1cm. For 75˚ and 83˚, the planning system over predicted the dose at superficial depths (0.1cm-0.3cm) by as much as 7%.

Conclusions: The results of this work indicate that the planning system under predicted the dose at the surface and superficial depths (depths ≤ 0.3cm) from a static TomoTherapy beam at both normal and oblique incidence by more than 5%.

Chapter 1: Introduction

I. Background and Significance

A. TomoTherapy

1. Introduction to the Hi•Art Delivery System

The TomoTherapy Hi•Art system is a relatively new radiation therapy treatment modality which has come into use in the treatment of various malignant lesions. This system offers a unique way of delivering radiation therapy as well as having the benefit of image-guided radiation therapy.

The TomoTherapy unit consists of a linear accelerator (linac) mounted onto a computed tomography (CT) ring gantry. This system is operational as a therapeutic delivery system and an imaging system. The incoming electron beam is incident onto a high atomic number target to create bremsstrahlung x-rays having a spectrum of energies from zero MeV up to the maximum accelerating potential of the system. The nominal energy of the x-ray beam within the treatment modality is 6 MeV with this energy stepped down to 3.5 MeV within the imaging modality. The linac is located 180˚ from an arc of detectors that is used in acquiring a megavoltage CT (MVCT) scan of the patient. The MVCT is done prior to treatment to localize the treatment area and re-position the patient if necessary. In addition, the detectors are active during the actual treatment of the patient and produce a sinogram of transmitted data resulting from the patient treatment.

Helical tomotherapy is a result of the gantry rotating about the patient as the couch moves continuously into the treatment unit. From the patient's eye view, the source of radiation spirals about them in a helical path. The couch moves into the unit through a bore which is 85 cm in diameter. The gantry's axis of rotation is 85 cm from the x-ray source in the center of the bore (Mackie et al., 2003).

A picture of the TomoTherapy unit along with the International Electrotechnical Commission (IEC) table (X_t, Y_t, Z_t) coordinate system is shown in Figure 1. The IEC table coordinate system is used in accordance with IEC Report 61217 (2002). When viewed from the foot of the couch, the positive Z_t axis runs vertically upward from the table top, perpendicular to the axis of the couch. The positive Y_t axis runs longitudinally toward the bore of the gantry, parallel to the axis of the table top. The positive X_t axis runs laterally toward the right side of the couch. The gantry rotates clockwise with respect to the viewer and is at 0˚ when a ray from the center of the bore to the source is directed upward, perpendicular to the axis of the couch. Unless otherwise noted, (X, Y, Z) in the rest of this document will refer to the IEC table coordinate system.

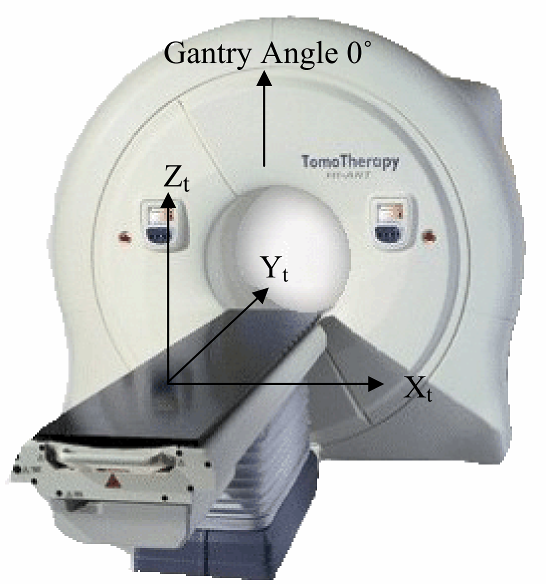

Figure 1. Picture of the TomoTherapy unit with the IEC table coordinates and gantry angle 0˚ defined.

The field length of the radiation beam (i.e., the length in the Y dimension) is defined by the secondary collimators or jaws. During treatment planning, the jaw positions are selected from a few discrete settings to produce field lengths of 0.6, 1.0, 2.5 or 5.0 cm at the axis of rotation. At Mary Bird Perkins Cancer Center (MBPCC), the two jaw selections available at the time of this study were 2.5 and 5.0 cm. The actual full-width-half-maximums of the beam longitudinal profiles as measured at the time of commissioning are 2.45 and 4.98 cm, respectively. The field length is kept constant throughout the helical delivery.

The field width of the radiation beam (i.e., the width in the X dimension for a gantry angle 0˚ beam) is defined by a multi-leaf collimator (MLC) with 64 leaves. At the axis of rotation, the projected-width of each leaf is 0.625 cm. When all of the MLC leaves are kept open, the maximum field width is 40 cm at the axis of rotation. The TomoTherapy MLC system is binary in that each leaf position is either open (i.e., out of the way of the beam) or closed (i.e., blocking the beam). The leaf open time is varied to achieve non-uniform beam intensities (as a function of gantry angle and couch position) for intensity modulated radiation therapy (IMRT) (Mackie et al., 2003). Shown in Figure 2, is a schematic of the MLCs showing both their ‘open’ and ‘closed’ states.

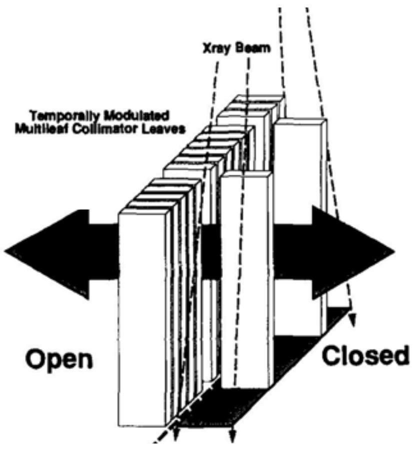

Figure 2. Illustration of TomoTherapy’s binary multi-leaf collimator leaves. (Mackie et al., 1993)

TomoTherapy is unique in the design of its beam filtration system in the treatment head. Conventional accelerators have a flattening filter downstream of the target. The filter is used to produce a uniform photon beam at a depth of 10 cm. TomoTherapy's treatment head does not have a flattening filter (Jeraj et al., 2004). The filter was considered unnecessary as TomoTherapy is a dedicated IMRT system. In the event that a uniform field is desired at a particular depth, it is possible to intensity modulate the beam to be so. A cross-sectional diagram of the TomoTherapy treatment head is shown in Figure 3. The unit does have a set of uniform thickness filters that provide electronic buildup to the monitor chambers (which monitor the output of the machine) and filter low-energy photons from the beam (Mackie et al., 2003).

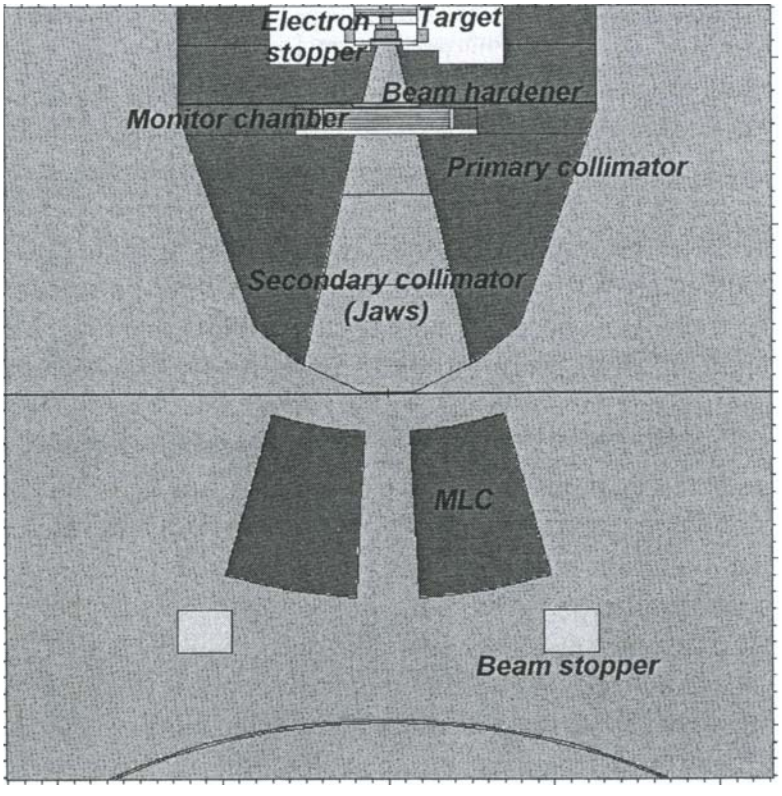

Figure 3. Diagram of the TomoTherapy treatment head. (Jeraj et al., 2004)

The TomoTherapy treatment system is designed to optimize the MLC leaf open times (i.e., beam weight) for 51 gantry angles or projections per rotation. A projection is a radiation beam directed onto the patient from a particular orientation (gantry angle and couch position). The treatment couch moves continuously into the bore during treatment at a rate determined by the gantry rotational period, the jaw width and the pitch. Pitch is the ratio of the distance traveled by the couch per rotation to the width of the jaw (at the axis of rotation). Typical values for pitch for a treatment delivery are between 0.2 and 0.5 (Mackie et al., 2003).

2. Introduction to the Treatment Planning System

The TomoTherapy treatment planning system offers several optimization techniques to achieve the desired dose to a specified target. The method used in this work was beamlet optimization. A beamlet is defined as the portion of a radiation beam from a single projection which passes through one open MLC leaf. Thus, there are 64 possible beamlets for each projection. With a beamlet calculation, the planning system first determines which beamlets pass through any structures defined as tumors. The corresponding leaves that produce these beamlets are set to be open, and their open times are varied during the optimization process. All other leaves are set to be closed (i.e., their beamlets have zero weight).

Dose is calculated separately for each beamlet and then summed to acquire the total dose from 51 projections times the number of rotations in the planned delivery. The projections are modeled as static beams. The gantry continuously moves while radiation is being delivered from beamlets within a projection, but the planning system models this as if the gantry stops to deliver each projection.

The dose calculation uses a convolution/superposition method and it can be broken up into two parts: the TERMA (total energy released per unit mass) calculation and the convolution/superposition energy deposition (Lu et al., 2005). The TERMA calculation models the transport of primary photons as they interact with the medium. The resulting TERMA dose grid is then convolved with dose kernels which are predictions of energy deposition from charged particles set in motion by primary photon interactions (Mackie et al., 1988). This convolution is performed using the following equation:

$$D(\vec{r}) = \int \frac{\mu}{\rho}(\vec{r}\,')\Psi_P(\vec{r}\,')A(\vec{r}-\vec{r}\,')d^3r' = \int T_P(\vec{r}\,')A(\vec{r}-\vec{r}\,')d^3r' \qquad (1)$$

where $D(\vec{r})$ is the dose at point $\vec{r}$, $\frac{\mu}{\rho}(\vec{r}\,')$ is the mass attenuation coefficient for the tissue at $\vec{r}\,'$, $\Psi_P(\vec{r}\,')$ is the primary photon energy fluence, and $A(\vec{r}-\vec{r}\,')$ is the dose kernel. $T_P(\vec{r}\,')$ is TERMA, the product of the mass attenuation coefficient and the photon energy fluence (Mackie et al., 2000).

Both the primary energy-fluence attenuation and the superposition with dose kernels are done on a voxel-by-voxel basis. The calculations incorporate the radiological path length traversed by radiation using voxel densities obtained from CT data (Balog et al., 1999). The convolution equation when corrected for radiological path length is as follows:

$$D(\vec{r}) = \int T_P(\rho_{\vec{r}\,'} \cdot \vec{r}\,')A(\rho_{\vec{r}-\vec{r}\,'} \cdot (\vec{r}-\vec{r}\,'))d^3\vec{r}\,' \qquad (2)$$

where $\rho_{\vec{r}\,'} \cdot \vec{r}\,'$ is the radiological path length from the source to the primary photon interaction site and $\rho_{\vec{r}-\vec{r}\,'} \cdot (\vec{r}-\vec{r}\,')$ is the radiological path length from the site of primary photon interaction to the site of dose deposition. The dose kernel $A(\rho_{\vec{r}-\vec{r}\,'} \cdot (\vec{r}-\vec{r}\,'))$ is calculated by range scaling dose kernels that are generated in water by the electron densities of the medium (Mackie et al., 2000).

Equation 2 is restricted to describing monoenergetic beams when in fact the primary photon beam is polyenergetic. The energy spectrum must be incorporated into the dose kernels. If variations in the incident spectrum are not significant, a kernel can be composed for the spectrum by the weighting the kernel at each energy by its contribution to the spectrum (Mackie et al., 1985).

The TomoTherapy beam model assumes the incident beam is comprised only of photons and does not include electron contamination in its dose calculating algorithm. For conventional linear accelerators, treatment planning systems that incorporate a convolution/superposition algorithm can use an empirical model to add electron contamination dose to the photon dose at superficial depths (Mackie et al., 2000).

3. TomoTherapy as a Superficial Treatment

TomoTherapy is currently being used primarily to treat a variety of deep-seated tumors. As the TomoTherapy system does not have an electron beam modality, as do traditional linear accelerators, it is important to know TomoTherapy's ability and potential for treating superficial diseases, which are often treated with electron beams. Recent studies have reported on the use of TomoTherapy as a treatment for superficial disease sites. Orton et al. (2005) used helical tomotherapy to deliver tangential photon beams to the scalp in order to avoid field matching issues associated with overlapping electron and photon fields (Tung et al., 1993). Ashenafi et al. (2006) compared TomoTherapy treatments plans for irradiation of the chest wall post-mastectomy to conventional treatment plans employing a combination of electron and photon beams. Both studies reported that the TomoTherapy planning system is capable of creating treatment plans that deliver a homogeneous dose to these superficial targets while sparing adjacent critical structures.

Neither study performed measurements to determine the accuracy of the computed doses. If helical TomoTherapy is to be used as a superficial treatment, it is essential that the treatment planning system accurately predicts the dose to the surface and superficial depths.

4. Previous Measurements – Serial Tomotherapy

Superficial dose distributions have been measured previously for a serial tomotherapy delivery to a superficial target. Mutic et al. (1999) used a PEACOCK planning and delivery system (NOMOS Corporation) along with a Varian 6 MV Clinac 600C/D to deliver serial tomotherapy. They used LiF thermoluminescent chips and an Exradin parallel-plate chamber to make measurements at the surface of a cylindrical phantom. The results of the study showed that the treatment planning dose calculation was not in good agreement with the measured dose at depths < 10 mm as shown in Figure 4. The treatment planning system's calculated dose overestimated the measured dose at depths ≤ 1 mm. The calculated dose also indicated that the superficial target was under-dosed by 15% at depths between 3-6 mm while the measured dose shows the superficial target receiving a full dose (approximately 100%) beyond 3 mm. The study suggested using a thin piece of bolus in the build-up region in treating superficial patient targets because of this discrepancy.

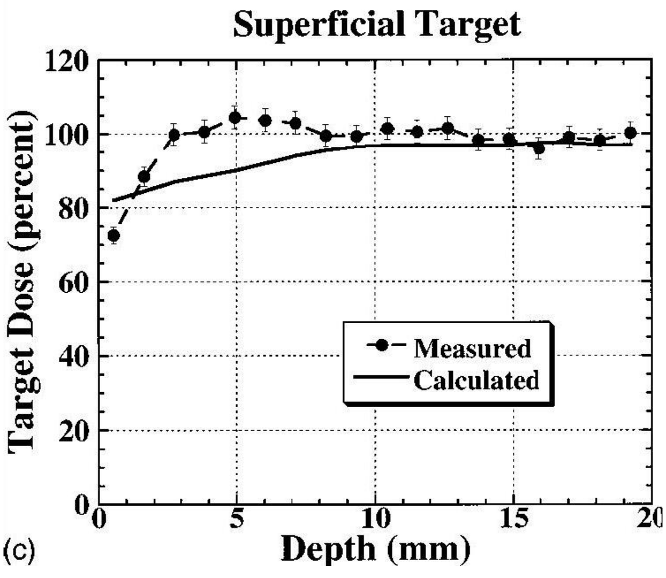

Figure 4. Comparison of calculated and measured superficial depth doses for the treatment of a superficial target in a phantom using serial tomotherapy. (Mutic et al., 1999)

It is important to note that the algorithm used to calculate dose in the Mutic study differs from that used by TomoTherapy. The PEACOCK treatment planning system's dose calculation algorithm incorporates a modified finite size pencil beam (FSPB) model (Low et al., 1998). The TomoTherapy treatment planning system uses a convolution/superposition method (c.f., Chapter 1, Section I.A.2) to calculate dose, which is expected to be more accurate.

5. Investigation of Static Beams

Since a TomoTherapy delivery is helical in nature, it is most important to study superficial dose from a helical treatment. Recent works have compared the treatment planning system's dose calculation to measurements for superficial targets in phantom (Cheek et al., 2006, Mitchell et al., 2006). Their results indicate discrepancies between calculated and measured doses at the surface and superficial depths.

A helical TomoTherapy superficial treatment is inherently complex. For the dose to be delivered accurately to a superficial target, many components of the system (e.g., MLCs, couch and gantry) must move in exact synchrony. The timing of each component must also be correctly predicted by the planning system. There are also factors involved in intensity modulation which could impact a superficial dose delivery (e.g., leaf latency, leaf transmission and inter-leaf leakage). These factors must be accurately modeled by the planning system as well. If a discrepancy existed between measured and calculated dose from a helical superficial treatment, it would be unclear as to what part of the measurement or model was the source of the error. Therefore, it was decided to study superficial dose from a static TomoTherapy beam (i.e., the gantry and table are stationary). In this way, it can be determined whether the planning system is accurately modeling the superficial dose from a single beam before determining whether it accurately models the dose from an entire helical superficial treatment.

A superficial TomoTherapy treatment will likely be a summation of beams that are both normal and oblique to the skin surface. Thus, this work concentrates on measuring and modeling the dose from a static TomoTherapy beam at normal and oblique incidence.

B. Surface Dose

1. Origin of Surface Dose

Dose to the skin surface in a normally incident megavoltage photon beam is the sum of two components. The first component is electrons created from photon interactions in the patient. Most of these electrons are scattered in a forward direction because they are created from primary photons traveling in a forward direction. However, some of these electrons may side scatter or back scatter to the surface. The second component of surface dose is electrons created from photon interactions prior to the patient. These electrons are created somewhere in the treatment head or the air column above the patient. They deposit their energy at the surface and superficial depths. These electrons are called contaminant electrons.

In an obliquely incident megavoltage photon beam, dose to the skin surface is still a sum these two components, but now forward scattered electrons created in the patient also reach the point of measurement at the surface. A diagram depicting the two components of surface dose for a normally and obliquely incident photon beam is shown in Figure 5.

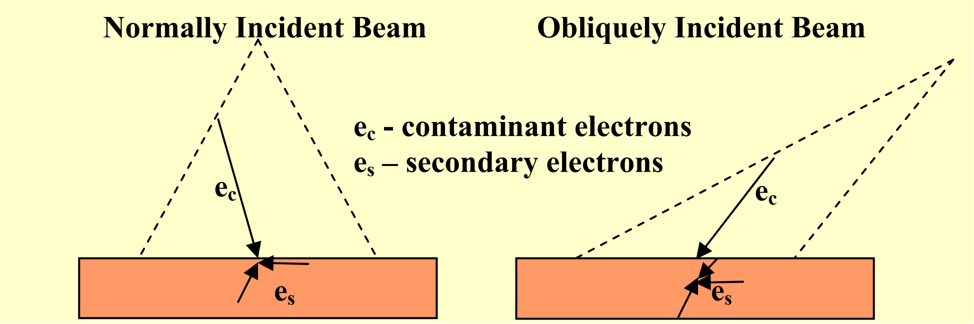

Figure 5. Diagram of the components which contribute to surface dose in a normally and obliquely incident photon beam.

2. Factors that Effect Surface Dose

a. Electron Contamination

For conventional linear accelerators, the dependence of electron contamination on the flattening filter and beam energy has been studied by several groups (Biggs et al., 1983, Jursinic et al., 1996, Kim et al., 1998, Lamb et al., 1997, Malataras et al., 2001, Yorke et al., 1985). Biggs et al. (1983) determined the contribution of electron contamination to dose at the skin surface by placing a dipole magnet in the path of various energy photon beams (10, 15 and 25 MV) for both Varian and Siemens accelerators. The field strength produced by the magnet was sufficient to deflect all electrons of energy ≤ 9 MeV out of the path of the beam. Using several parallel-plate chambers, they compared relative surface charge for measurements with and without the magnet in place for a 10x10 cm^2 field. They found that for the 10 MV beam there was a small, statistically-insignificant difference in the charge measured at the surface with and without the magnet. However, for the 25 MV beam, there was as much as a 20% difference in the charge measured at the surface. This would imply that in low energy photon beams, fewer contaminant electrons are being created in the treatment head or in the air below it.

Malataras et al. (2001) studied the influence of electron contamination with various therapeutic energies and in different geometries by doing Monte Carlo simulations on two linear accelerators, Saturne-25 and Saturne-41. Their results show that the main sources of contaminant electrons are the flattening filter and the air below it. The air produces electrons of low energies of which the mean of the energy spectra vary from 1 to 2 MeV, depending on the nominal energy of the photon beam. The flattening filter produces a wide energy spectrum of electrons similar to the bremsstrahlung spectrum. The study predicts that although the flattening filter may serve as a source of contaminant electrons, it may also serve to absorb electrons generated in the target, primary collimator and the air inside the head. They found that as the nominal energy of the photon beam increases (> 12 MV) the flattening filter begins to dominate as the source of contaminant electrons. At 6 MV, however, the air below the accelerator generates the majority of contaminant electrons.

Superficial dose increases significantly with increasing field size. As the field dimensions increase, the dose in the build-up region increases (Khan, 2003). For small field sizes, most contaminant electrons created in the treatment head or the air below scatter out of the field. Kim et al. (1998) studied surface dose for an 8 and 18 MV photon beam as a function of field size, source to surface distance (SSD), off-axis distance, acrylic block tray, wedge (external and dynamic), and MLCs. They found that for an open 8 MV beam, 9x9 cm^2 field size, the skin dose was approximately 10% of the maximum dose. In this study, nothing was done to quantify the amount of superficial dose contributed by contaminant electrons.

The maximum field size for a static TomoTherapy beam is 40x5 cm^2 as defined by the secondary collimating jaws. The equivalent square of this field size is approximately an 8.3x8.3 cm^2 field (Day et al., 1995), which is a relatively small field.

During a typical TomoTherapy delivery, the table moves longitudinally through the bore as many projections are made onto the patient. Contaminant electrons that scatter out of a small field may scatter onto other portions of the patient's surface and contribute to surface dose in that area. Thus, even though the field size of each projection may be small, the equivalent field size of all projections may be large.

b. Oblique Incidence

The effect of obliquely incident beams may increase the dose at the surface of a patient in a composite helical delivery. For superficial tumors, it is likely that the composite dose from a helical delivery will include beams directed at both normal and oblique incidence. Obliquely incident photon beams can reduce the skin-sparing effect and increase dose at the skin surface as compared to normally incident beams. For obliquely incident beams, the surface dose can be a function of both scattered electrons from the air and the accelerator, and forward, back, and side scattered electrons produced in the phantom material (Gerbi et al., 1987).

3. Measurement of Surface Dose with Parallel-Plate Chambers

a. Over-Response

Dose in the build-up region is often measured using a parallel-plate chamber. A thin entrance window allows measurements to be taken practically at the surface of a phantom. However, parallel-plate chambers with a fixed electrode separation allow contributions to the chamber signal from electrons scattering into the collecting volume from the side walls (Rawlinson et al., 1992), especially in oblique beams (Gerbi et al., 1997). With parallel-plate extrapolation chambers, on the other hand, a signal is collected for different electrode separations and extrapolated to a zero electrode separation, thus eliminating the side wall contribution. It is generally accepted that extrapolation chambers provide the most accurate means of measuring dose at the surface and in the buildup region. However, these chambers are very expensive and are tedious and time-consuming to use. For these reasons, it is common to use parallel-plate chambers with a finite electrode separation to measure dose at the surface and in the buildup region of megavoltage photon beams (Rawlinson et al., 1992).

The Attix chamber (Model 449) available from Gammex/Radiation Measurements, Inc. (RMI) was specifically designed to overcome the shortcomings common to fixed electrode separation parallel-plate chambers. The Attix chamber is a parallel-plate chamber with a thin Kapton™ collecting window of 4.8 mg•cm^{-2}, a small collecting volume of 0.125 cm^3, an inner wall diameter of 40 mm and a small electrode separation of 1 mm (Gerbi, 1993). Rawlinson et al. (1992) studied the over-response of parallel-plate chambers in the build-up region by comparing data from an extrapolation chamber to data from parallel-plate chambers. They found that in order for the over-response of a parallel-plate chamber to be less than 1.5%, the ratio of wall diameter (*w*) to electrode separation (*s*) should be at least 23 for electrode separations of 1-4 mm. The Attix chamber exceeds this ratio with a (*w/s*) of 40. Gerbi (1993) compared the response of the Attix chamber, and several other commercially available parallel-plate chambers, to that of an extrapolation chamber in both normal and oblique photon beams at the phantom surface for a 5x5 cm^2 field. In comparison to other parallel-plate chambers, the Attix chamber shows a small amount of over-response at 0° which varies little up to a beam angled at 75° with a maximum over-response of 1.12. This is illustrated in Figure 6.

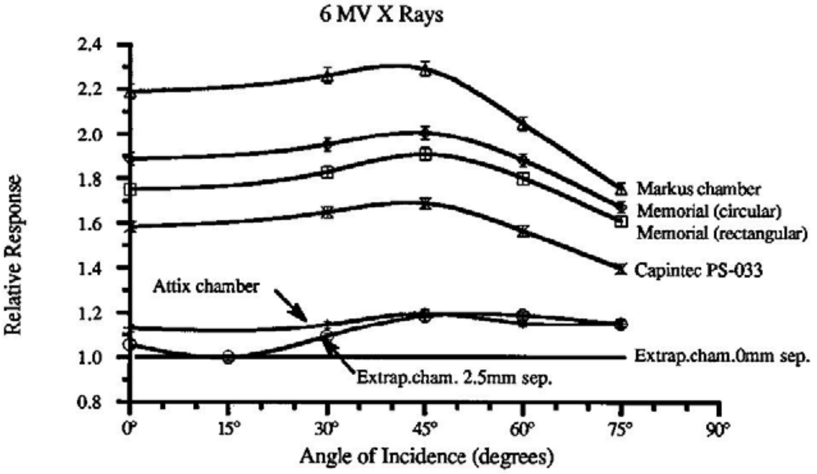

Figure 6. The response of the Attix chamber, and various other chambers, at several oblique angles, relative to the response of an extrapolation chamber for a 6 MV beam. (Gerbi, 1993)

b. Polarity Effect

The polarity effect of parallel-plate chambers can be significant in the build-up region with up to a 30 % difference in collected charge taken at positive and negative bias voltages

(Gerbi, 1993, Gerbi et al., 1987). The polarity effect exists because charge collected by an ion chamber changes in magnitude when the collecting voltage is reversed. The change in magnitude is a result of high energy electrons producing a current that is independent of gas ionization. The extra current results in an addition or reduction of the collector current, depending on the polarity of the collecting voltage being applied. Current collected outside the sensitive volume can also cause a polarity effect. This current is highly dependent on the design of the chamber and increases in areas where electronic equilibrium is not reached (Khan, 2003). However, the Attix chamber exhibits only a small polarity effect, less than 3.5% at depths from the surface to d_{max} (the depth of maximum dose) (Gerbi, 1993). The polarity effect can be eliminated by averaging the absolute value of the difference of the readings taken at opposite polarity, keeping the sign of the readings intact (Gerbi et al., 1987).

II. Hypothesis and Specific Aims

• Hypothesis

Superficial doses measured along the central axis from a static TomoTherapy beam agree with doses calculated by the TomoTherapy planning system to within 5% (of the maximum dose) for angles of incidence 0˚- 83˚.

• Specific Aims

Aim 1. Measure the Superficial Dose from a Static TomoTherapy Beam at Normal and Oblique Incidence:

Measure the dose using a parallel-plate chamber at depths ≤ 2 cm on the central axis for a static TomoTherapy beam with a field size of 40x2.5 cm^2 and 40x5 cm^2 at normal incidence and oblique angles up to 83˚ for multiple source to detector distances.

Aim 2. Compare Measurements of Superficial Doses with a Parallel-Plate Chamber to Measurements with TLDs at Normal and Oblique Incidence:

Measure the dose at depths ≤ 2 cm at normal and oblique incidence for a static TomoTherapy beam with a field size of 40x2.5 cm^2 and 40x5 cm^2 using TLDs. Compare these measurements with those taken in Aim 1 using a parallel-plate ionization chamber.

Aim 3. Compare the Measured Superficial Doses to TomoTherapy's Model for a Static Beam Delivery:

Use the TomoTherapy treatment planning system to calculate single static beams and compare calculated to measured doses.

Chapter 2: Methods and Materials

I. Aim 1

A. Measurements of Static Beams

1. Measurement Conditions

Dose was measured on the central axis for static 40x2.5 cm^2 and 40x5 cm^2 normally and obliquely incident TomoTherapy beams. The delivery system was operated in 'physics' mode which allows beams to be delivered while the gantry and table are stationary. Data was collected at superficial depths ($\leq$ 2 cm).

Ionization charge was measured using a Gammex/Radiation Measurements, Inc. (RMI) Model 449 parallel-plate ionization chamber, otherwise known as the Attix chamber, connected to a Keithley Model 602 electrometer with a digital readout. The Attix chamber has a 1 mm electrode separation, a 12.7 mm diameter collector, a 0.125 cm^3 collecting volume, a 13.5 mm guard ring width, and a 4.8 $mg \cdot cm^{-2}$ Kapton™ entrance window. A cross-sectional diagram of the Attix chamber is shown in Figure 7.

A bias voltage of -300 V was applied to the collecting electrode of the Attix chamber for data collected at all depths. A positive and negative bias voltage (+300 V/-300 V) was applied to collect data at the surface due to the polarity effect of the chamber (c.f., Chapter 2, Section I.D.1). The leakage associated with this system was less than $3x10^{-14}$ amperes.

The chamber was embedded into a 2.5 cm thick piece of RMI Model 457 Solid Water® so that the entrance window of the chamber was flush with the surface of the phantom. The chamber was kept at a constant source to chamber distance (SCD) for all measurements. Phantom material of varying thickness was added above the chamber to increase the depth of measurement. Thus, adding material to increase depth, decreased the source to surface distance (SSD) for the measurement. Phantom material (6-10 cm) was placed beneath the chamber piece to serve as backscatter material.

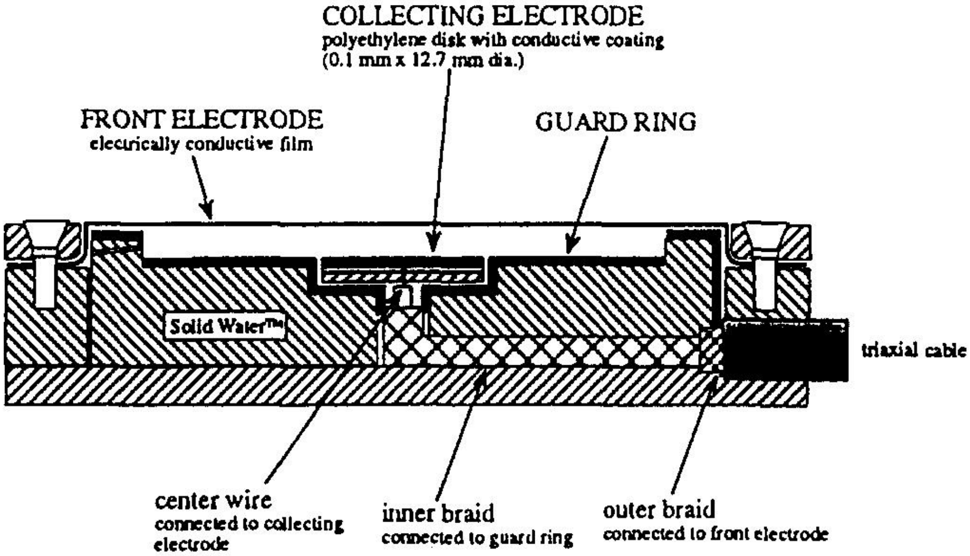

Figure 7. Cross-sectional diagram of the Attix chamber (Gammex/RMI Model 449) showing its major components. (Attix, 1993)

To account for machine output changes, each ionization reading collected was normalized to the number of monitor units delivered. All monitor unit normalization was done using monitor chamber #1 in the treatment head. At least three normalized readings were averaged for each depth. For normal incidence, readings were recorded and converted into percent depth doses (PDDs) using the following equation:

$$PDD = \frac{\langle Rdg / MU \rangle_d}{\langle Rdg / MU \rangle_{d_0}} * \left(\frac{SSD + d_0}{SSD + d}\right)^2 * 100\% \qquad (3)$$

where $\langle Rdg / MU \rangle_d$ is the average normalized reading taken at depth d. In this work a normalization depth, d_o, of 1.5 cm was used. For oblique incidence, readings were recorded and converted into PDDs using the following equation:

$$PDD = \frac{\langle Rdg/MU \rangle_{d}^{\theta}}{\langle Rdg/MU \rangle_{d_o}^{\theta=0}} * (\frac{SSD + d_0}{SSD + d})^2 * 100\% \qquad (4)$$

where $\langle Rdg/MU \rangle_{d}^{\theta}$ is the average normalized reading taken at depth *d* for angle of incidence θ at $\approx$ 70 cm SCD and $\langle Rdg/MU \rangle_{d_o}^{\theta=0}$ is the average normalized reading taken at the normalization depth, d_o, for a normally incident beam at 70 cm SCD. The inverse square term in Eq. 3 and 4 is needed to correct for the change in SSD introduced by adding phantom material above the chamber which is held at a constant SCD.

2. Measurement of Normally Incident Beams

Superficial doses were measured for normally incident beams at 55, 70 and 85 cm SCD. The phantom and chamber were placed onto the TomoTherapy couch so that the chamber was at the virtual isocenter position (70 cm from the axis of rotation, in the –Y direction). The fixed position green lasers are used to setup this position. The phantom is kept at this position for the measurement of a beam at 85 cm SCD. To achieve the shorter SCDs (70 and 55 cm), the couch is moved up (+Z direction) so that the chamber is at the desired distance from the source. A picture and diagram of this setup is shown in Figure 8.

3. Measurement of Obliquely Incident Beams

Superficial doses were measured for obliquely incident beams at nominal angles of 30˚, 45˚, 60˚, 75˚ and 83˚ from normal incidence. The phantom and chamber were placed at an angle relative to the central axis of the beam.

For a static beam delivery, the gantry angle is limited to the cardinal angles (0˚, 90˚, 180˚ and 270˚) to deliver a beam. Due to this feature, wedged Styrofoam supports were constructed so that the phantom material could be angled toward the beam. The blocks were constructed to achieve the desired angles mentioned above. To verify the angle of incidence, a narrow field

(1.2×5 cm^2) was used to expose an EDR2 film which was taped to the side of the angled phantom (perpendicular to the surface of the phantom). The top of the phantom was marked on the film. The angle between the top of the phantom and the center of the radiation beam was confirmed for every angle of incidence measured.

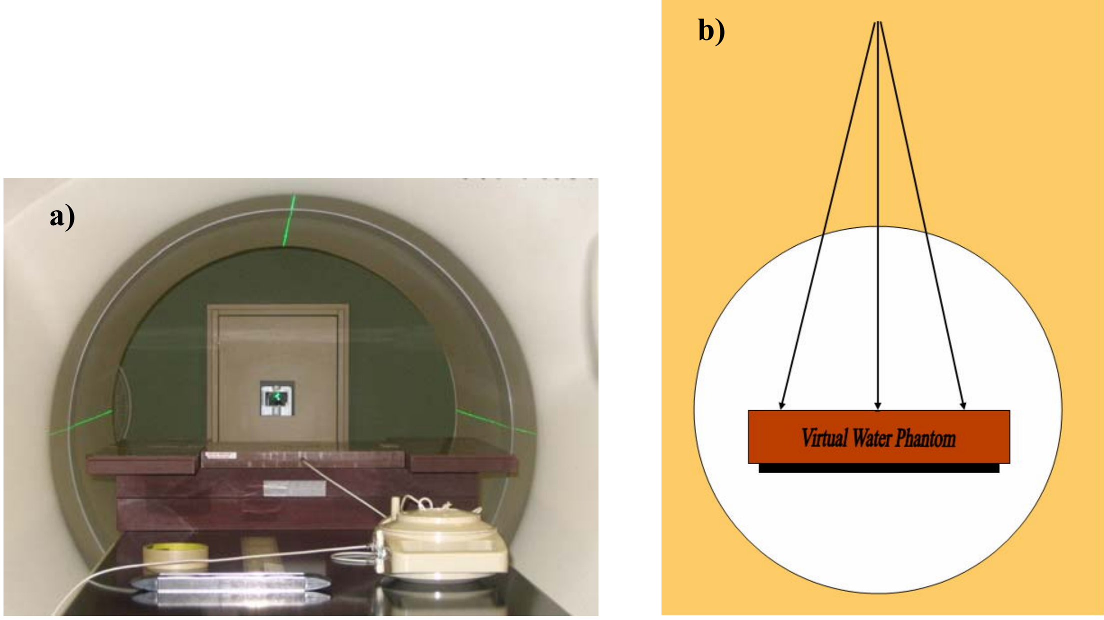

Figure 8. Picture (a) and diagram (b) of the setup for the measurement of normally incident beams.

All of the oblique measurements were made at or near 70 cm SCD. This distance was chosen to simulate a typical SSD found in treatments for clinical TomoTherapy patients. However, there was a limitation in achieving 70 cm SCD with some of the oblique angles. The width of the phantom had to be large enough to encompass the width of the beam (40 cm at the axis of rotation) at the surface. The bore is only 85 cm in diameter, so when the phantom is placed at an angle and moved toward the source, there is a possibility that the edge of the phantom will collide with the bore edge. Thus, measurements for incident nominal angles $\geq 60^\circ$ were made as close to 70 cm SCD as could be achieved so that the full width of the phantom would fit inside the bore.

For incident angles of 30˚ and 45˚, the gantry was set to deliver a beam at 0˚ with the phantom tilted toward the beam. A picture and diagram of this setup at a 45˚ angle of incidence is shown in Figure 9. For incident angles ≥ 60˚, the gantry was set to deliver a beam at 90˚ with the phantom tilted toward the beam. A diagram and picture of the setup at a 60˚ angle of incidence is shown in Figure 10.

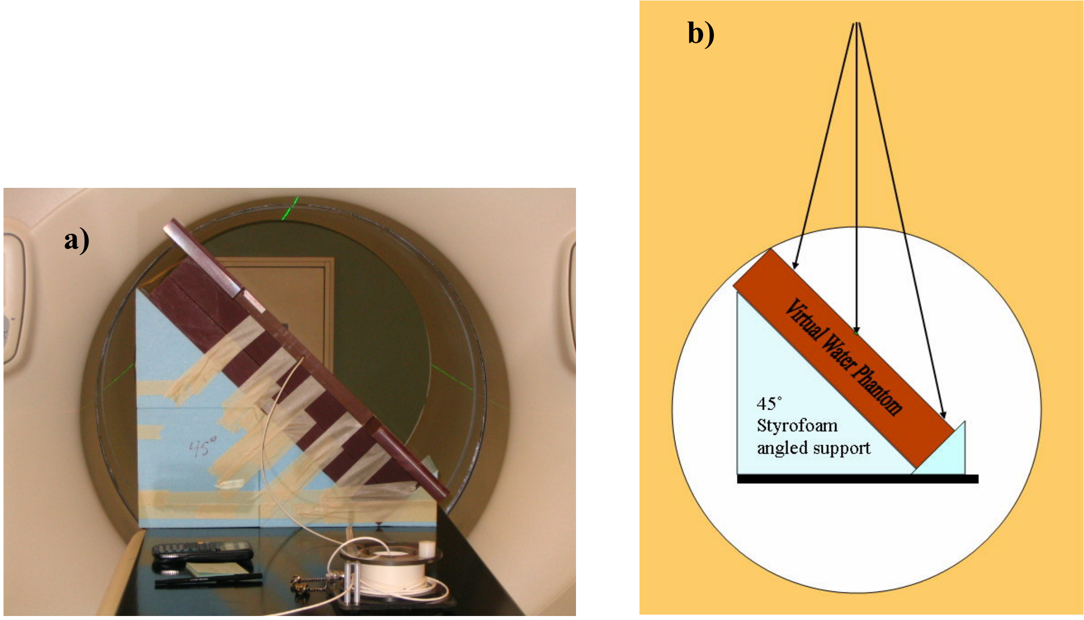

Figure 9. Picture (a) and diagram (b) of the setup for the measurement of a 45˚ angled beam.

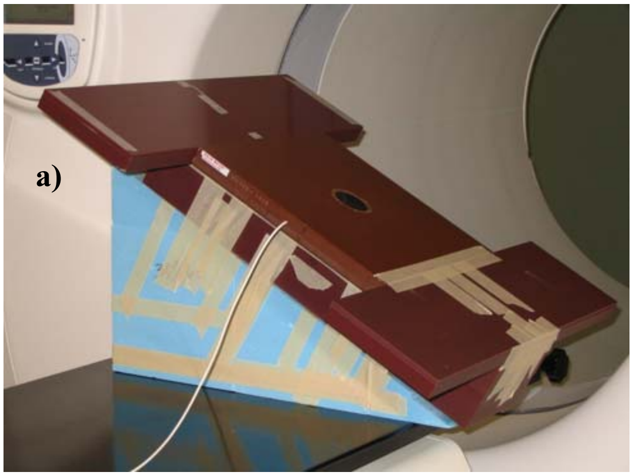

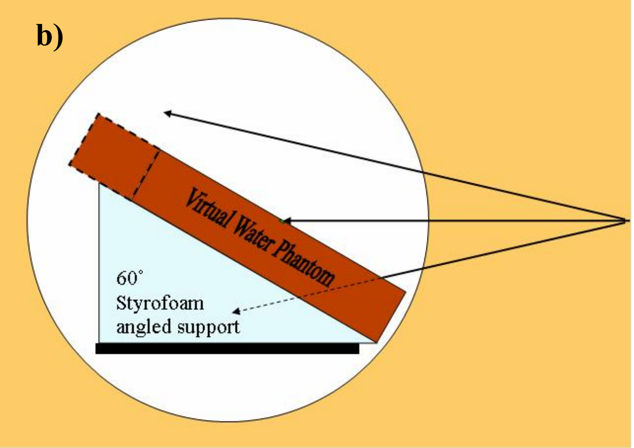

Figure 10. Picture (a) and diagram (b) of the setup for the measurement of a 60˚ angled beam.

B. Measurements of Phantom Material Thickness

Several pieces of phantom material were used to create depth for the measurements described above. Both CIRS Plastic Water® and Standard Imaging Virtual Water® slab phantoms were used. The thickness of each piece less than or equal to 1 cm was confirmed by measurement.

The Plastic Water® slab phantoms used were 30x30 cm^2 and ranged from 0.1 to 0.5 cm in thickness. Tello et al. (1995) measured and found the density of this material to be 1.014 g•cm^{-3} ± 1.1%. They also measured the thickness of these slabs using a micrometer and found that the maximum difference in thickness measured anywhere on the slab was 0.2 mm.

The Virtual Water® slab phantoms used were 55x15 cm^2 and were 1 cm thick. The manufacturer states that the density of this material is 1.03 g•cm^{-3}. They also quote the error in thickness to be ± 0.15 mm.

The thickness of each piece was determined using a KANON Vernier caliper. This caliper has a 10 cm jaw depth. Each slab of phantom material was placed within the jaws of the caliper so that the jaws were fully extended over the piece of material. In this setup, it was assumed that the resulting measurement was of the maximum thickness of the portion of material enclosed in the jaws. Several measurements were done in this manner for each piece of phantom material. The Vernier caliper was capable of determining thickness to within 0.02 mm.

For the Virtual Water® pieces, the jaws of the caliper were long enough to extend to and include the center portion of the slab. For the Plastic Water® pieces, the jaws of the caliper were not long enough to extend to the center portion of the slab. Thus, a dial indicator was also used to confirm the measurements for the Plastic Water® pieces.

A dial indicator measures displacement rather than thickness and can determine whether there is any variation across a piece of phantom material. The dial indicator was mounted onto a magnetic stand which was supported by lead weights so that the tip of the indicator was touching a flat counter top. The counter was determined to be level using a bubble level. The dial was set to zero at the counter top and then the displacement was measured when a piece of phantom material was placed beneath the tip. A single measurement was taken at the center of the piece. The variation in thickness was determined by moving the piece around in an ≈ 3 cm radius about the center and observing the dial for changes. This device was used to measure only the pieces of Plastic Water® with quoted thicknesses of 5 mm or less. The dial indicator was capable of measuring displacement to within 0.01 mm. A picture of the setup is shown in Figure 11.

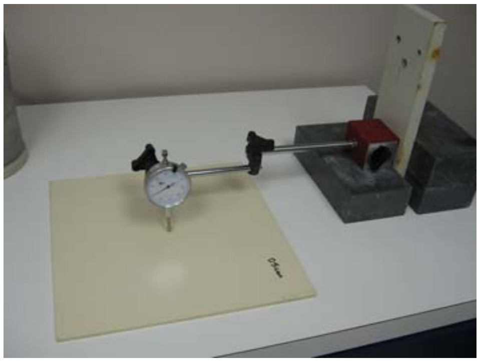

Figure 11. Picture of the setup for the measurement of the thickness of phantom material pieces using a dial indicator.

A summary of measurements made with the Vernier caliper and the dial indicator is shown in Table 1. The quoted thickness is the manufacturer's specification for the thickness of each piece. The error in the Plastic Water® pieces is from a previous measurement of this material (Tello et. al., 1995). The error in the Virtual Water® pieces was quoted by the manufacturer. The error in the measured thickness was determined by the standard deviation of the measurements. The results of the measurements made with the dial indicator are similar (within the error of the quoted thickness) to those made with the Vernier caliper for the Plastic Water® pieces.

Table 1. Thickness of phantom material pieces measured with the Vernier caliper and the dial indicator.

CIRS Plastic Water® 30x30 cm^2

Piece #	Quoted Thickness [cm]	Measured Thickness [cm] Vernier Caliper	Measured Thickness [cm] Dial Indicator
1	0.10 ± 0.02	0.102 ± 0.002	0.102 ± 0.003
1	0.20 ± 0.02	0.205 ± 0.001	0.206 ± 0.003
2	0.20 ± 0.02	0.203 ± 0.002	0.203 ± 0.003
3	0.20 ± 0.02	0.203 ± 0.002	0.203 ± 0.004
1	0.50 ± 0.02	0.501 ± 0.001	0.503 ± 0.005

Standard Imaging Virtual Water® 55x15 cm^2

1	1.00 ± 0.02	1.001 ± 0.002
2	1.00 ± 0.02	0.992 ± 0.005

In order to make measurements at a number of different depths, the phantom material pieces were used alone or stacked together. All of the depth dose data have been plotted versus the combined depth of phantom material determined from the Vernier caliper data. The depths used and their associated error are shown in Table 2. The depth is a summation (if two or more pieces were stacked together) of the average measurement for that piece. The error associated with each depth was determined using the standard deviation from the measurement of each piece combined in the method of quadratic summation.

Table 2. Summary of depths used in depth dose profiles. These were determined by measuring the thickness of phantom material pieces used to create depth.

Depth [cm]
0.102 ± 0.002
0.204 ± 0.002
0.306 ± 0.003
0.501 ± 0.001
0.705 ± 0.002
0.807 ± 0.002
0.996 ± 0.004
1.098 ± 0.004
1.200 ± 0.004
1.302 ± 0.004
1.497 ± 0.004
1.701 ± 0.004
1.993 ± 0.005

C. Measurements of Inverse Square

Percent depth dose data were extracted from data measured at a constant source chamber distance by multiplying by an inverse square correction as in Eq. 3 and 4. The inverse square law says that the intensity of radiation is proportional to the inverse of the distance squared from a point source. Deviations from the inverse square law in a photon beam can arise due to scattered photons from the treatment head (rather than primary photons from the target) contributing to the overall photon fluence (McKenzie et al., 1993). When this occurs, an effective source position can be determined which takes into account that the position of the source may ‘appear’ to be different than the physical position due to scattered photons.

To confirm the inverse square law with a TomoTherapy system, output data were measured by placing a cylindrical ionization chamber in a static 40x5 cm^2 beam at various SCDs. Ionization charge was measured using a Keithley Model 602 electrometer and a PTW Farmer chamber, Model N30010, with a 3.2 cm diameter Acrylic buildup cap. This chamber has a 0.6 cm^3 collecting volume. The chamber and buildup cap were attached to an acrylic support stand

and positioned off the end of the couch to minimize scatter radiation. Static beams were delivered and ionization charge was measured for 65, 70, 75, 85 and 90 cm SCD.

The chamber was first placed at virtual isocenter using the fixed green lasers. The lasers were aligned to a line on the buildup cap demarcating the center of the volume (in the X direction). An MVCT was then done to ensure that the chamber was at the isocenter position. The chamber required a 2 mm shift in the Z direction so that the active volume would be at isocenter. To ensure that the entire volume of the chamber was in the beam, the chamber was placed so that the long axis of the chamber was parallel to the long axis of the radiation beam. To ensure that the chamber was centered within the radiation beam in the Y direction, a piece of EDR2 film was placed distal to the chamber when the chamber was at 85 cm SCD. Once it was determined that the chamber was at isocenter and centered in the beam, the chamber was not moved and the other SCDs were achieved by moving the couch in the Z direction, keeping the Y position fixed. Pictures of the chamber setup are shown below in Figure 12.

Three ionization readings were collected and normalized to the number of monitor units delivered. The inverse square root was taken of the average of the normalized readings and plotted against the distance from the source.

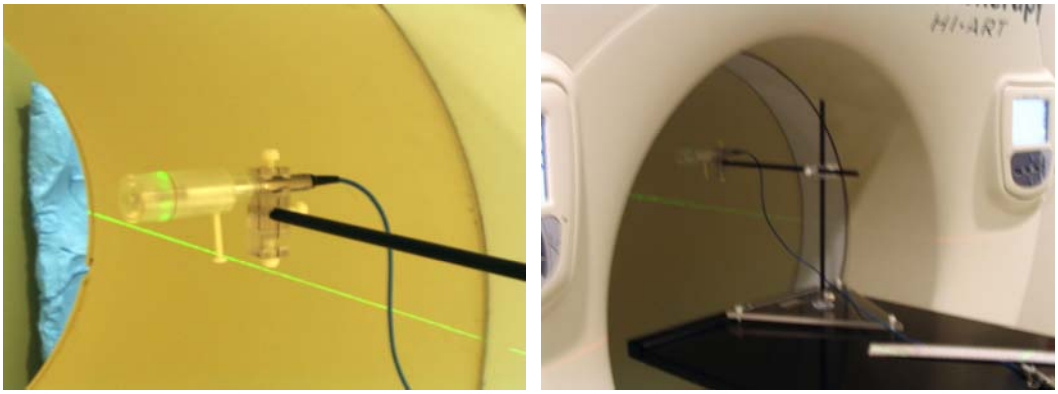

Figure 12. Pictures of the setup used to measure output versus distance from the source for a TomoTherapy beam.

A plot of the inverse square of the output (average normalized reading) versus distance from the source for a TomoTherapy beam is shown in Figure 13. The data taken at various distances from the source were fitted with a line. Note that when the linear fit is extrapolated back to the x-axis, the x-intercept is 0.0 ± 0.1 cm (85 cm from isocenter) indicating that the effective and physical source positions are the same since isocenter is 85 cm from the source with the TomoTherapy system. The linear relationship in the data verifies that the output varies according to the inverse square of the distance from the physical source.

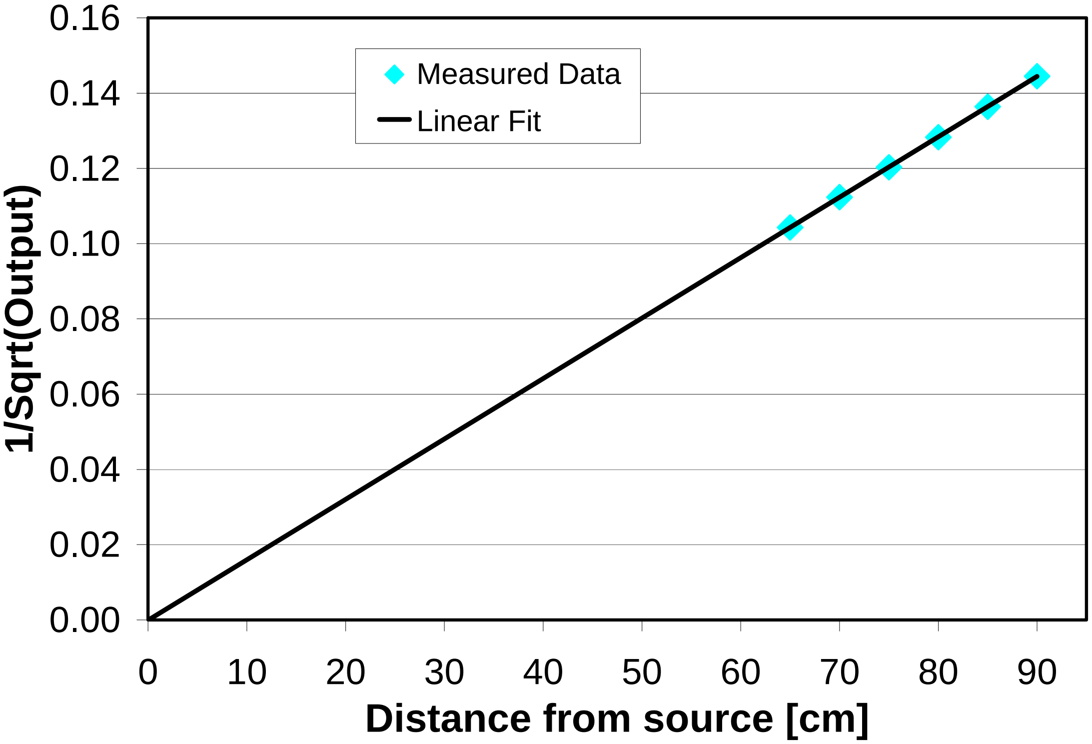

Figure 13. Plot of the inverse square of the output for a static TomoTherapy beam versus distance from the source.

D. Attix Chamber Measurements

1. Polarity Effect

Measurements were taken to quantify the polarity effect of the Attix parallel-plate chamber. Readings were taken at the surface and 0.1 cm depth under various measurement conditions with both a positive and negative chamber bias. A summary of the measurements is shown in Table 3. The maximum polarity effect, defined by the deviation of the absolute value of the ratio of readings from unity taken with opposite polarities (-Rdg/+Rdg), was found to occur at the phantom surface. This is consistent with studies done on the Attix chamber by Gerbi (1993). Because of the polarity effect of this chamber, ionization charge at the surface was determined by taking the average of the readings measured at both a positive and negative bias voltage. Since the polarity effect is not significant at depth, ionization charge at depth was taken as the reading measured with a negative bias voltage only.

Table 3. Measurements taken to quantify the polarity effect of the Attix parallel-plate chamber.

SCD [cm]	Angle of Incidence	Depth [cm]	|-Rdg/+Rdg|
75	0°	0.0	0.96
90	0°	0.0	0.96
50	0°	0.0	0.96
75	83°	0.0	0.99
75	0°	0.1	0.99
90	0°	0.1	0.99
50	0°	0.1	0.99
75	83°	0.1	1.00

2. Cross-Calibration of Chamber

For the purposes of making a comparison between measured and calculated data, it was necessary to convert ionization readings taken with the Attix chamber to dose. In order to obtain an absorbed-dose-to-water calibration factor, $N_{D,w}^{Q}$, in accordance with the AAPM TG-51 calibration protocol, the Attix parallel-plate chamber was cross-calibrated with a cylindrical chamber. The cross-calibration method used is similar to that recommended by TG-51 (Almond et al., 1999) and TG-39 (Almond et al., 1994). An Exradin cylindrical chamber (Model A1SL) was used for cross-calibration with the Attix chamber. The A1SL has a 0.056 cm^2 collecting volume, with a 0.2 cm radius and a 0.44 cm long cylindrical cavity.

The cross-calibration was done in a static TomoTherapy beam at a depth of 1.5 cm. TG-39 recommends intercomparing a parallel-plate chamber with a cylindrical chamber at a depth that ensures charged particle equilibrium and excludes electron contamination. The depth chosen was sufficient to ensure that none of the cylindrical chamber volume was in a high dose gradient region. The A1SL cylindrical chamber and the Attix parallel-plate chamber were placed at this depth for every measurement condition and field size investigated.

The Attix chamber exhibits a known over-response relative to data obtained from an extrapolation chamber (c.f., Chapter 1, Section B.3.a). This over-response is a function of incident angle (c.f., Figure 6). By cross-calibrating the Attix chamber to the cylindrical chamber at normal and oblique incidence, the angular response of the Attix chamber is removed as a factor in the calculation of dose.

The diameter of the collecting volume of the Attix chamber is 1.27 cm. With the 5.0 cm jaw, the longitudinal length of the beam profile (at the SCDs measured) is sufficient to cover the entire volume of the chamber with a uniform dose. However, with the 2.5 cm jaw, this is likely not the case, since the edges of the chamber are located in the shoulders of the beam profile, as shown in Figure 14. By cross-calibrating the Attix chamber to the cylindrical chamber with both field sizes, the volume effect of the Attix chamber is removed as a factor in the calculation of dose.

The longitudinal length of the volume of the cylindrical chamber is 0.44 cm. It is assumed that the longitudinal length of the beam profile is sufficient to cover the entire volume of the chamber with a uniform dose for both jaw sizes, as shown in Figure 14. It is also assumed that the chamber exhibits a uniform response across the collecting volume and that the chamber is perfectly centered within the beam. It is possible, however, that there is a slight volume effect with the cylindrical chamber with the 2.5 cm jaw as well. This effect is expected to be small (< 0.5% of the dose output), but since the cylindrical chamber is used to calibrate the Attix chamber, if the response is low for the cylindrical chamber, it would cause the Attix chamber data to be low as well.

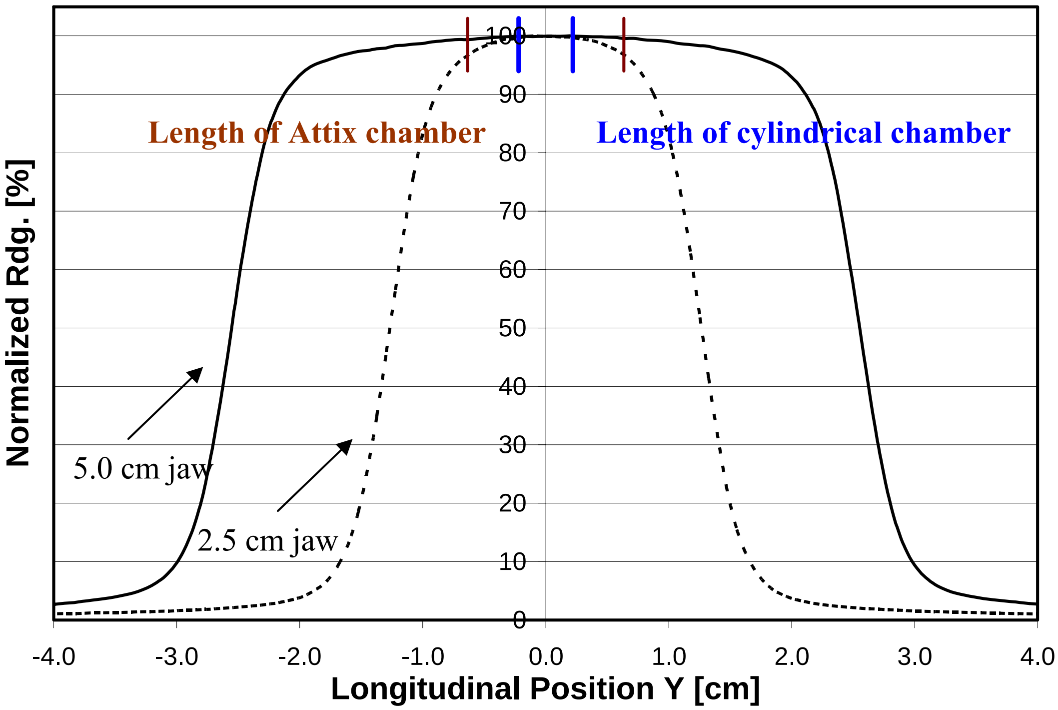

Figure 14. The active longitudinal length of both the cylindrical chamber and the Attix chamber overlaying the longitudinal beam profiles for the 2.5 and 5.0 cm jaws, showing the volume of both chambers within the shoulders of the profiles.

According to TG-51, charge collected by an ion chamber in a photon beam of beam quality Q can be converted to dose in water, D_w^Q, using the following equation:

$$D_w^Q = M * N_{D,w}^Q \tag{5}$$

where M is the fully corrected ionization reading, and $N_{D,w}^{Q}$ is the absorbed-dose-to-water calibration factor in a beam of quality Q. The ionization reading is corrected for ion recombination, temperature and pressure variations, inaccuracy of the electrometer if calibrated separately from the ion chamber, and chamber polarity effects.

Dose was calculated according to Eq. 5 using the A1SL cylindrical chamber at a depth of 1.5 cm for each measurement condition (i.e., field size and incident angle). This dose was compared to the response of the Attix chamber at a depth of 1.5 cm for the same measurement condition.

A field size, fs, and incident angle, θ, absorbed-dose-to-water calibration factor, $\widetilde{N}_{D,w}(fs,\theta)$, was determined for the Attix chamber in a TomoTherapy beam by relating dose calculated with the cylindrical chamber to the response of the Attix chamber according to the following:

$$\widetilde{N}_{D,w}(fs,\theta) = \frac{D_{w}^{A1SL}(fs,\theta)}{M^{Attix}(fs,\theta)} \tag{6}$$

where $D_{w}^{A1SL}(fs,\theta)$ is the dose calculated with the A1SL cylindrical chamber at a depth of 1.5 cm for a particular measurement condition and $M^{Attix}(fs,\theta)$ is the fully corrected ionization reading from the Attix chamber under the same measurement condition at a depth of 1.5 cm. $\widetilde{N}_{D,w}(fs,\theta)$ is similar to $N_{D,w}^{Q}$, defined by the TG-51 protocol, but also includes corrections for angular dependent over-response and detector volume. $\widetilde{N}_{D,w}(fs,\theta)$ is then used in Eq. 5 to calculate dose with the Attix chamber at other depths for each measurement condition. Table 4 shows $\widetilde{N}_{D,w}(fs,\theta)$ for each measurement condition.

Table 4. Summary of calibration factors used to convert ionization to dose as a function of field size and incident angle.

	$\widetilde{N}_{D,w}(fs,\theta)[cGy/nC]$	
SCD, θ	**40x5 cm^2**	**40x2.5 cm^2**
85 cm, 0°	33.2	34.6
70 cm, 0°	33.6	35.7
55 cm, 0°	34.1	39.2
70 cm, 30°	33.5	36.4
70 cm, 45°	33.4	36.5
73 cm, 60°	32.9	38.2
75 cm, 75°	32.5	36.2
75 cm, 83°	33.5	36.1

II. Aim 2

A. TLD Measurements

1. Measurement Conditions

Superficial dose was measured on the central axis for 40x5 cm^2 and 40x2.5 cm^2 static TomoTherapy beams using thermoluminescent dosimeters (TLDs). Measurements were made at depths ≤ 2 cm for beam angles of 0°, 60°, 75° and 83°. The TLDs were used to measure dose at shallow depths (< 0.5 cm) and at a depth of 1.5 cm. The TLDs were placed at a constant source to detector distance while phantom material of varying thickness was used to create depth. Phantom material (6-10 cm) was used beneath the TLDs to provide backscatter.

LiF TLD-100 powder purchased from REXON TLS Systems, Inc. was used. The TLD powder was sealed in a cellophane packet as shown in Figure 15. Each packet contained approximately 40 mg of powder spread evenly over an approximately 1 cm^2 area in the packet in an attempt to create an even layer. Two packets of TLD powder were irradiated, one at a time, for each irradiation condition. Phantom material was placed on top once the powder was spread out in as uniform a layer as possible.

Figure 15. Picture of a TLD packet (LiF powder enclosed in a cellophane wrapper) used in measurements.

Packets of TLD powder were irradiated to known doses above and below the expected measured doses to establish a calibration curve. One packet was not irradiated to determine the background signal.

2. Reading of TLDs and Conversion to Dose

The TLD samples were read using a REXON UL-320 TLD Reader. A Mettler Electronic Analytical Balance was used to determine the mass of each powder sample that was read. The TLD powder in each packet was divided into 3 approximately equal samples to measure thermoluminescence. The sample of powder was loaded onto a planchet and the planchet with powder was weighed on the balance and then placed into the reader. For each sample, the thermoluminescence (TL) or the photon count from the glow curve was recorded along with the mass of the sample. A net TL per mass, $(TL/mass)_{net}$, was found by subtracting the TL per mass of the background sample, $(TL/mass)_{bkg}$, from the TL per mass of the sample.

A calibration dataset was obtained by finding a $(TL/mass)_{net}$ for known doses that extend above and below the expected dose from the measurements. The output of the TomoTherapy beam was first measured under reference conditions (5x10 cm^2 field, 75 cm SSD, and depth of 10 cm) using protocol for the monthly quality assurance test of output. Next, static beams were delivered to the calibration TLD packets under the same reference conditions that output was measured, with specific treatment times in order to produce the desired dose. Based on the number of monitor units delivered and the output measurement, the dose to each packet was determined and used to develop a calibration curve.

Data were collected on three different occasions for the different angles and field sizes measured; therefore, three different calibration datasets were obtained. The calibration curves were used to determine the dose for each TLD dataset and are shown in the Appendix. For each calibration dataset, a second-order polynomial fit was applied to the data and unknown doses were found by interpolating using this fit. Extrapolation was not needed as the range of known doses covered the range of unknown.

3. Determination of Plotted Depths

The dose measured in each TLD packet represents an average of the doses deposited within the volume of powder. Since the powder was not arranged in a monolayer within the packet, the measurement represents an average of doses obtained at different depths within the packet. Assuming the depth dose varied linearly through the packet, the measurement represents the dose at an average depth.

To determine the average depth within a TLD packet, a dial caliper was used to measure the thickness of several packets. The dial caliper was capable of measuring thickness to within 0.01 mm. The thickness of the powder itself with its cellophane wrapper, $\tau_{wrapper+TLD}$, was determined. From this, an effective depth, $d_{eff,TLD}$, was determined which represented the depth at which the dose was equal to the average dose deposited in the TLD powder. It was estimated to be at a point which was half the thickness of the powder plus packet ($d_{eff,TLD} = \tau_{wrapper+TLD} / 2$).

Measurements were taken to determine the effective density of the TLD powder. TLD-100 powder is a mixture of LiF crystals and air. LiF has a density of 2.64 g/cm^3 but the effective density of the powder may be different because of the mixture of air and crystals. To determine the effective bulk density, a lump of TLD powder was placed into a planchet of known volume, V. The mass, m, of this volume of powder was then measured using the Mettler electronic balance. From this, an effective density, ρ_{TLD}, was estimated to be 1.2 g•cm^{-3}.

The effective depth, $d_{eff,TLD}$, was converted to a water-equivalent depth by scaling by the ratio of the electron density of LiF to the electron density of water, $\rho_{e,TLD} / \rho_{e,H_2O}$. The equations which represent how the effective depth in water was determined are as follows:

$$\rho_{TLD} = \frac{m}{V} \tag{7}$$

$$d_{eff,H_2O} = d_{eff,TLD} * \frac{\rho_{e,TLD}}{\rho_{e,H_2O}} \tag{8}$$

$$\frac{\rho_{e,TLD}}{\rho_{e,H_2O}} = \frac{\rho_{TLD}(\frac{Z}{A})_{LiF} * N_A}{\rho_{H_2O}(\frac{Z}{A})_{H_2O} * N_A} \tag{9}$$

where Z and A represent the atomic number and mass number, respectively, of the denoted molecules and N_A is Avogadro's number.

A summary of measurements made to determine the effective bulk density of LiF TLD powder and the depth at which to plot the TLD data is shown in Table 5. The depth dose plots from the TLD measurements incorporate this effective depth, where the plotted depth would be the effective depth in water of the TLD powder, d_{eff,H_2O}, plus the thickness of phantom material added.

Table 5. Summary of measurements to determine the depth at which to plot the TLD data.

	Value
$\rho_{TLD}[g \bullet cm^{-3}]$	1.196 ± 0.058
$d_{eff,TLD}[cm]$	0.020 ± 0.005
$d_{eff,H_2O}[cm]$	0.020 ± 0.007

III. Aim 3

A. Simulated CT Datasets

1. Creating Images

In order to simulate static field measurements on the planning system, it was necessary to create CT datasets representing the phantom geometry. The phantom could have been scanned on a CT simulator, but this would have imposed a couple of limitations. First, the CT scanner has a maximum scanning field of view (FOV) of 50 cm. This would have been too small to scan the entire phantom for either the oblique angle or short SCD setups. Second, the simulated datasets could easily be manipulated to change the pixel resolution if so desired which was indeed the case. Thus, CT images used for the static beam treatment plans were artificially generated.

The simulated CT datasets were a representation of the phantom used to take measurements (e.g., a phantom placed 70 cm from the source and at a 45° angle). An in-house FORTRAN program was used to generate DICOM-compatible CT datasets for use in this study. The program used an Excel spreadsheet, which contained a 2D array of CT numbers for each slice, as input. The spreadsheets depended on the beam geometry, the number of pixels in the image, the field of view, and the density information contained in one slice of a CT image. The space occupied by phantom material was given a density of 1.0 g•cm^{-3} and the space around the phantom was given a density of 0.0 g•cm^{-3}. Since the phantom was uniform in the longitudinal direction, one unique spreadsheet was used to generate the number of slices representing the longitudinal length of the phantom.

For each image set, there were 62 slices spread 2.5 mm apart. Slices 1 and 62 were of zero density and were added to the inferior and superior ends of the phantom. The phantom was 15 cm in the longitudinal dimension and 55 cm in the transverse dimension, and this size was reproduced in slices 2-61 of the datasets. The phantom was of variable height depending on the amount of backscatter and the depth used in the measurement being modeled. A diagram illustrating this process is shown in Figure 16.

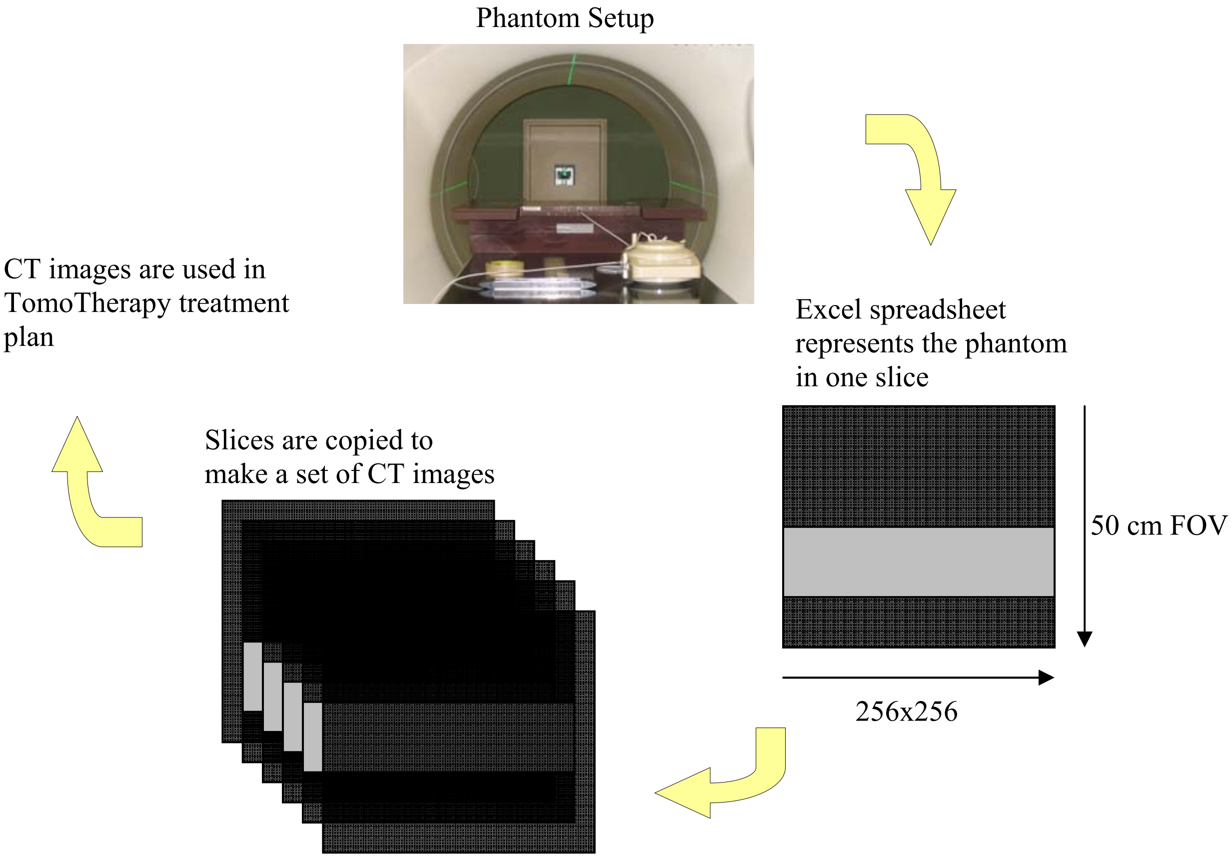

Figure 16. Diagram illustrating the process of creating CT images representing the phantom setup.

2. Creating Depth

For all measurements conditions, the ion chamber was positioned at a fixed location on the central axis of the beam. The front surface of the Attix chamber was taken as the depth of measurement, and measurements at increasing depths were made by adding phantom material on top of the chamber (i.e., the SCD stayed the same while the SSD changed). In order to simulate the same geometry in the planning system for the oblique measurement conditions, a separate CT dataset was created for each depth measured. The first dataset positioned the phantom such that the SSD was set equal to the SCD used in the measurement (e.g., 70 cm). The next dataset was the same as the first but with the density changed from 0.0 to 1.0 g•cm^{-3} in the first layer of pixels on top of the phantom. Since the position of the calculation point is the same, this change increases the depth equal to the size of one pixel. Each subsequent dataset had another layer of unit-density pixels added to the top of the phantom, until approximately 2.2 cm in depth was added to the first phantom.

3. Placement of Phantoms within Images

When CT images are transferred to the TomoTherapy planning system, the center of the image is taken as the center of rotation in the TomoTherapy system. For the normally incident beams, the CT dataset was simulated so that the top of the phantom was the appropriate distance away from the center of the image according to the SCD. For 85 cm SCD, the top of the phantom was placed in the center of the image. For 70 cm SCD, the top of the phantom was placed 15 cm above the center of the image. For 55 cm SCD, the top of the phantom was placed 30 cm above the center of the image.

For each obliquely incident setup, the top and center of the phantom was placed in the CT image so that it would be the appropriate distance away from the center of the image according to the SCD and the angle of incidence. An example is shown in Figure 17 for 70 cm SCD, 45˚ angle of incidence. The SCD is used to find, f, the distance from the center of the image to the top and center of the phantom. The angle of incidence is used to find the vertical and lateral movements to position the phantom as such.

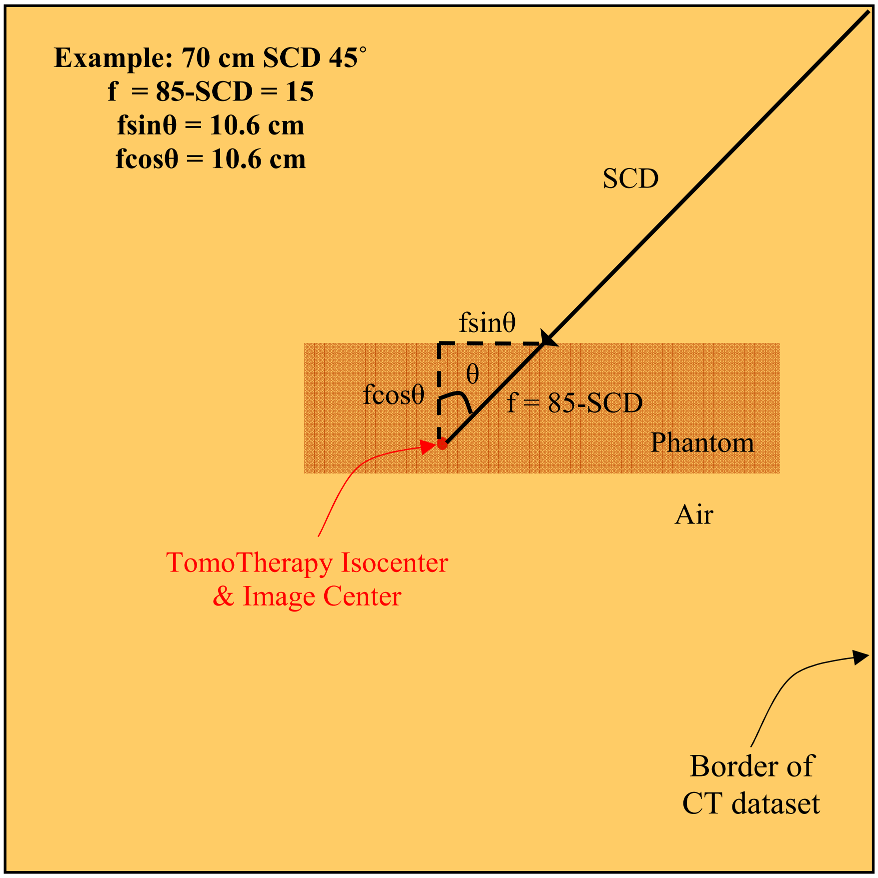

Figure 17. Diagram illustrating how the phantom is positioned in oblique angle setups. The example in the diagram is for the setup at 70 cm SCD, 45˚ angle of incidence.

4. Image/Dose Grid Resolution

A typical array size for a CT image is 512x512 pixels. The default setting of the TomoTherapy planning system is to down-sample imported CT images to an array size of 256x256. However, it is possible to change this setting within the planning system to keep the image at a 512x512 array.

There are several options for a dose grid resolution within the TomoTherapy planning system. A ‘fine’ dose grid was used for all calculations. With this dose grid resolution, dose is calculated to a matrix of points aligned with every voxel of the image set (i.e., the dose matrix matches the CT grid).

The field of view and the array size determine the voxel resolution which, in turn, determines the depth and depth increments that can be used. The convolution/superposition algorithm calculates dose to one point in every voxel. Thus, the voxel resolution governs how close to the surface the dose will be calculated.

For 85 and 70 cm SCD at normal incidence, a 50 cm FOV, a 512x512 array, and a fine dose grid were used which produces voxels of side length 0.098 cm (≈ 1 mm). This cuts off approximately 2.5 cm of the phantom on either lateral end (± X direction), but it was thought that the scatter from these portions would contribute insignificantly to the dose at the center of the phantom at shallow depths. For 55 cm SCD at normal incidence, a 62 cm FOV, a 512x512 array, and a fine dose grid were used which produces voxels of side length 0.121 cm (≈ 1.2 mm). This FOV was necessary in order to put the top of the phantom 30 cm anterior (+ Z direction) to the image center.

For all the oblique setups, a 100 cm FOV, a 512x512 array, and a fine dose grid were used which produces voxels of side length 0.195 cm (≈ 2 mm). This pixel resolution was used to calculate dose for all depths up to 2 cm because it encompasses the entire phantom. However, to calculate dose closer to the surface, a 50 cm FOV, a 512x512 array and a fine dose grid were used which produces voxels of side length 0.098 cm (≈ 1 mm). This FOV cuts off a lateral portion of the oblique phantoms on the same side as the source (+ X direction). A comparison between a dose point at depth with and without the lateral portion of the phantom cut off was made for 75 cm SCD, 83° angle of incidence. Cutting off this portion did not make a significant difference in the dose (< 1% difference between data points) reported at depth. This voxel resolution was only used to calculate dose within the first 3 mm of the phantom.

B. Static Beam Treatment Plans

1. Plan Parameters

The TomoTherapy treatment planning system (version 2.2) was used to calculate single static beams. The planning system sums the dose contribution from each projection in the sinogram. The first projection is defined with the central axis centered on the first CT slice and at the gantry start angle (default = 0°). The geometry of the remaining projections are determined by the number of projections per rotation (default = 51), the selected jaw width and pitch. To reduce the calculation time required, the number of projections per rotation was set to two for every phantom plan. The gantry start angle was changed to match the different angles of incidence.

The pitches were chosen so that one projection (projection number 13) would be centered longitudinally on the phantom, and directed at the desired gantry angle. For jaw widths of 2.5 or 5.0 cm, the pitch was set to 0.510 or 0.251, respectively. Using the chosen jaw widths and pitches and with two projections per rotation, the total number of projections used for each treatment sinogram was 24.

2. Replacing Sinogram Files

After the plan parameters were entered, beamlet optimization was initiated on the treatment planning system. Once all beamlets were calculated, optimization was interrupted and the phantom plan was archived. The file containing the optimized fluence sinogram was found within the archived data. This file contains the optimal leaf-open times for each projection. The file was replaced with a custom sinogram, generated using in-house software. The custom sinogram contained 24 projections. For the 13th projection in this sinogram, all of the 64 leaves were turned on (i.e., their leaf open times were set to one). All other projections in this sinogram were turned off (i.e., their leaf open times were set to zero).

Once the fluence sinogram was replaced, the phantom plan was restored and the dose calculation was continued. The planning system loaded the replaced sinogram and dose was calculated before further optimization could take place. A final dose calculation was performed so that dose and sinogram information could be extracted for each phantom setup.

C. Static Beam Model

1. Determining Depth and Shifting Data

The final dose calculation within the planning system produces an end-of-planning (EOP) dose file. The EOP file is a 3-D matrix with dose grid points located in each voxel of the CT image set. When the static beam calculation is complete, the dose grid points in regions of air (density = 0.0 g•cm^{-3}) report a dose of 0.0 Gy. The first dose grid point along the direction of the beam to report a non-zero dose is the first dose grid point located within the phantom (density = 1 g•cm^{-3}). There is only one dose point per voxel, and it is necessary to determine at what depth within the voxel and phantom this point represents.

As described in Chapter 1, Section I.A.2, the first part of the dose calculation with the convolution/superposition algorithm is to calculate the total energy released into the medium (TERMA) from primary photons. The result is a TERMA grid which describes how much energy is released in each voxel. Logically, a TERMA grid point would represent energy released at a point in the center of the voxel. The primary photons would have traversed and interacted with a thickness of material equal to half the voxel thickness. The TERMA does not change much over this region because the attenuation is small within a single voxel.

After the TERMA is calculated, convolution with the dose kernels is performed according to Eq. 2. Numerically, the convolution is performed by stepping along a finite number of rays ‘thrown’ from each TERMA grid point. This is illustrated in Figure 18 (a). For each voxel, the dose deposited is a summation of calculations done at each step along each ray passing through that voxel. In Figure 18 (a), 7 such rays are displayed, originating from the TERMA grid point which is centered in the voxel. In actuality, TomoTherapy integrates along 384 rays (24 zenith by 16 azimuthal angles) from each TERMA grid point.

In TomoTherapy’s implementation of the algorithm, however, the TERMA grid point is not located in the center of the voxel, but at the leading edge of the voxel (in the direction of the beam) (Schnarr and Olivera). The rays are thus ‘thrown’ from the front edge of the voxel as in Figure 18 (b) instead of the center as in Figure 18 (a).

Since the TERMA grid is shifted by a half-voxel length upstream, the dose grid is effectively reporting the dose shifted by a half-voxel length downstream. This can be seen by comparing the TERMA rays in Figures 18 (a) and (b). With the shifted TERMA grid (Figure 18 (b)), the convolution will over-estimate the dose in the first voxel, since each ray will spend more time and deposit more dose in the first voxel before moving to the next voxel. If the TERMA grid point were located in the center of the voxel, the effective depth, d_{eff}, would be half the length of the voxel, r/2, as in Figure 18 (a). With the TERMA grid point located at the front of the voxel, the depth is shifted by a half-voxel length to be at an effective depth equal to the length of the voxel, r, as in Figure 18 (b).

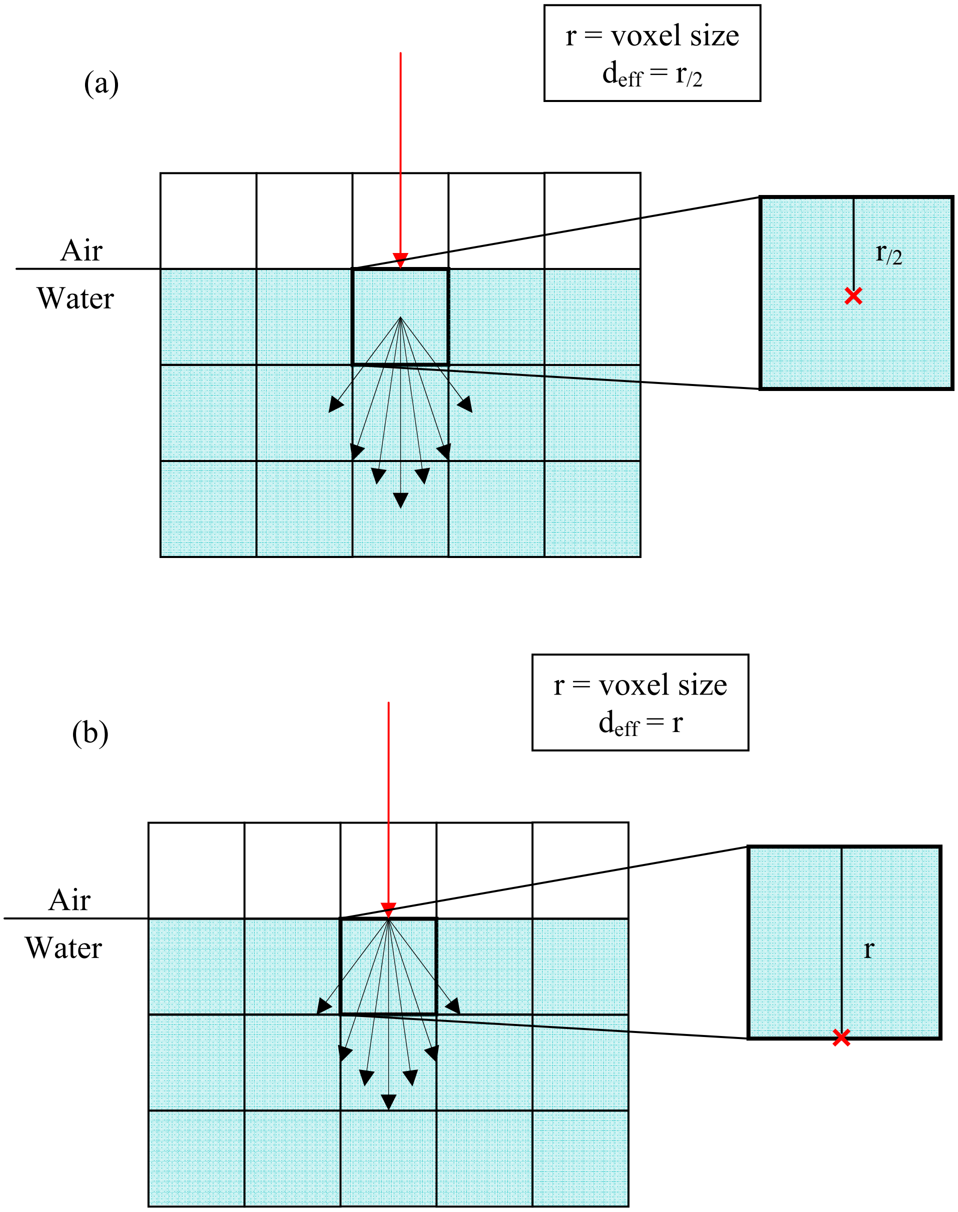

Figure 18. Diagram illustrating the effect of the TERMA dose calculation starting in the (a) center of a voxel and the (b) leading edge of a voxel in a normally incident beam.

Evidence for this shift in depth for a normally incident photon beam can be seen by comparing doses calculated at different voxel sizes. Figure 19 displays PDDs from a 40x5 cm^2 beam at 85 cm SSD, 0° angle of incidence, calculated with different dose grid resolutions. A fine dose grid was used for all calculations, but the resolution of the planning CT image sets was changed. The lowest resolution (voxels with side length = 2 mm) was created using a 50 cm FOV and a 256x256 array. The voxels with a side length of 1 mm were created using a 50 cm FOV and a 512x512 array. The voxels with a side length of 0.5 mm were created using a 25 cm FOV and a 512x512 array. The voxels with a side length of 0.25 mm were created using a 12.5 cm FOV and a 512x512 array. The latter two resolutions were accomplished by cutting off a portion of the radiation beam and phantom. Scatter from the lateral portions contributes little to dose at superficial depths and these phantom setups were used only for the purpose of finding the appropriate shift in depth.

Figure 19 (a) displays percent depth-dose data plotted with the first dose point being taken as the dose at an effective depth, d_{eff}, of half the size of the voxel, r/2. The data are plotted versus depth for each of the dose grid resolutions described earlier. There is disagreement in the data in Figure 19 (a) even though each dataset represents the same calculation parameters. Figure 19 (b) displays the same data, with the depth shifted by half the size of the voxel to account for the TERMA grid shift. As is evident from Figure 19 (b), the data now show the same results for the same simulation condition. Thus, in this study, the calculated depth dose plots were shifted a half-voxel length from the center of the voxel for the normally incident data.

In an obliquely incident beam, if the TERMA grid point was located in the center of the voxel, the rays would be 'thrown' from this location in the direction of the beam as illustrated in Figure 20 (a). The effective central axis depth would be the distance from where the beam enters the voxel to the center of the voxel. This distance is denoted as r_c. The corresponding perpendicular depth, d_{eff}, is r/2.

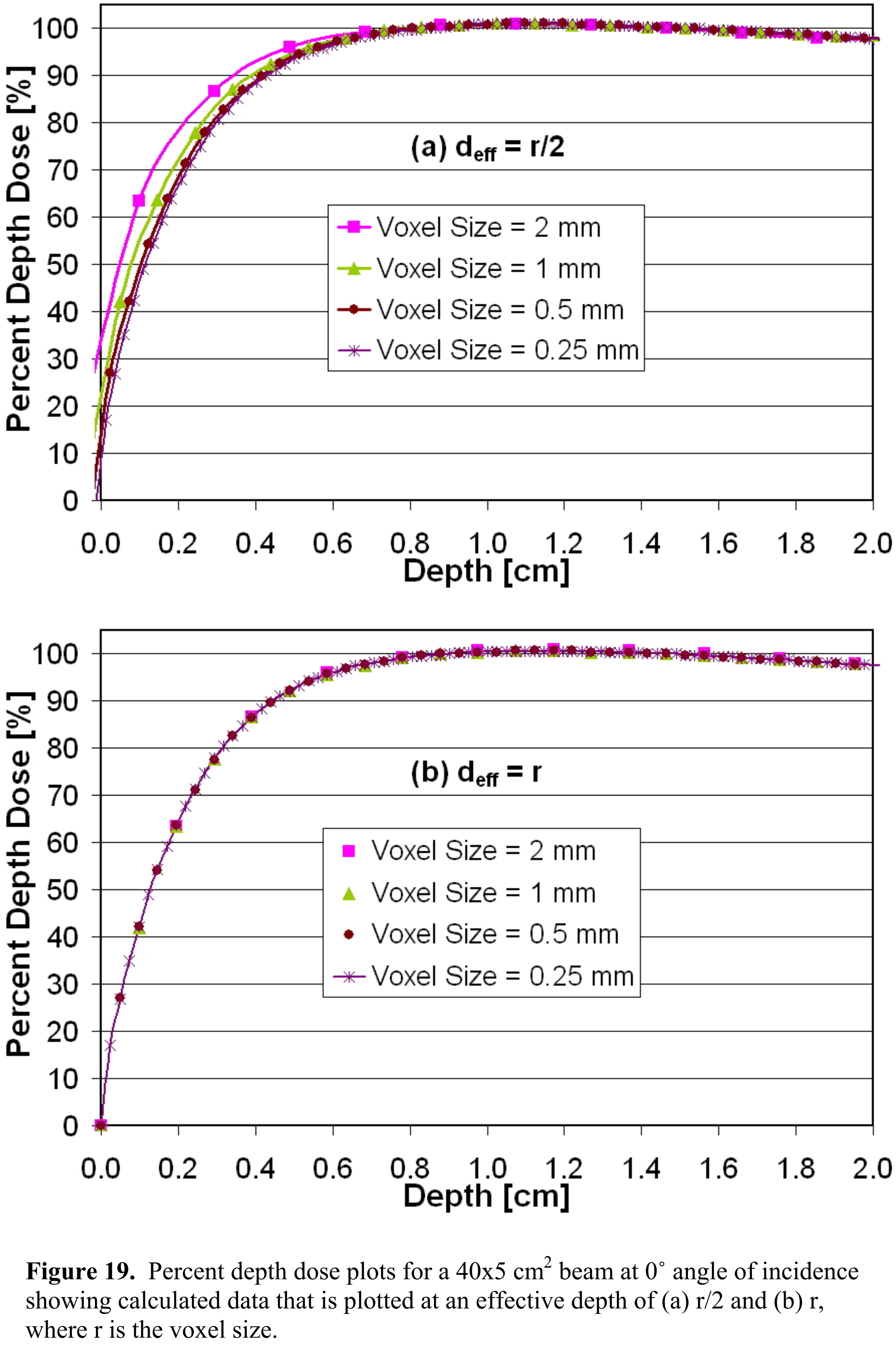

Figure 19. Percent depth dose plots for a 40x5 cm^2 beam at 0° angle of incidence showing calculated data that is plotted at an effective depth of (a) r/2 and (b) r, where r is the voxel size.

For oblique beams, since the TERMA grid point is shifted by a half-voxel length upstream, in the direction of the beam, the dose grid is effectively reporting the dose shifted by a half-voxel length downstream, in the direction of the beam, as in Figure 20 (b). The effective central axis depth is equal to the distance to the center of the voxel, r_c, plus a half-voxel length, r/2. The corresponding perpendicular depth, d_{eff}, is r/2*(1+cosθ).

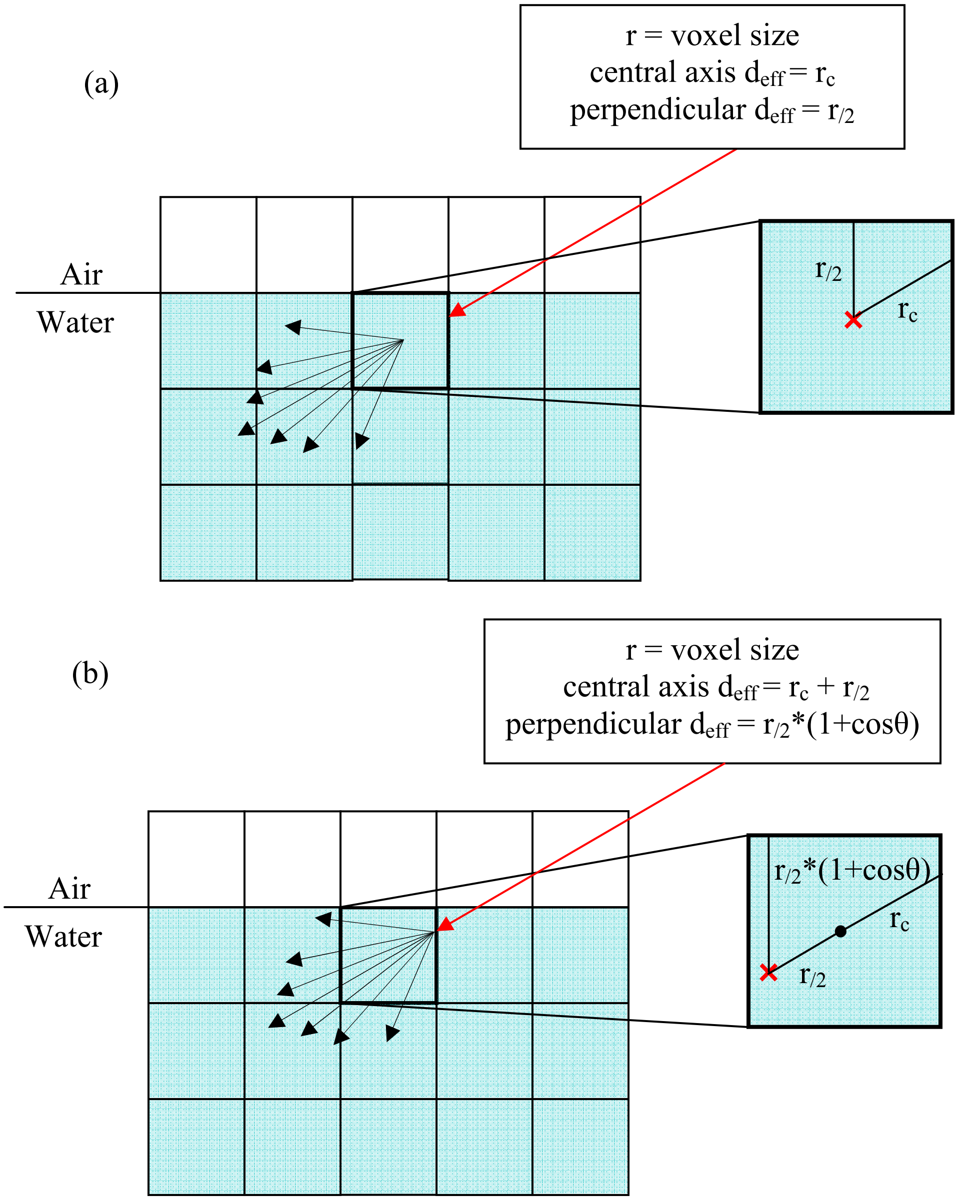

Figure 20. Diagram illustrating the effect of the TERMA calculation starting in the (a) center of the voxel and the (b) leading edge of a voxel in an obliquely incident beam.

Evidence for this shift in depth for obliquely incident beams is shown by comparing doses calculated at different voxel sizes. Figure 21 displays PDDs from a 40x5 cm^2 beam at 85 cm SSD, 45° angle of incidence, calculated with different dose grid resolutions. A fine dose grid was used for all calculations, but the resolution of the planning CT image sets was changed. The lowest resolution (voxels with side length = 4 mm) was created with a 50 cm FOV and a 128x128 array. The next resolution (voxels with side length = 2 mm) was created using a 50 cm FOV and a 256x256 array. The voxels with a side length of 1 mm were created using a 50 cm FOV and a 512x512 array. The voxels with a side length of 0.5 mm were created using a 25 cm FOV and a 512x512 array.

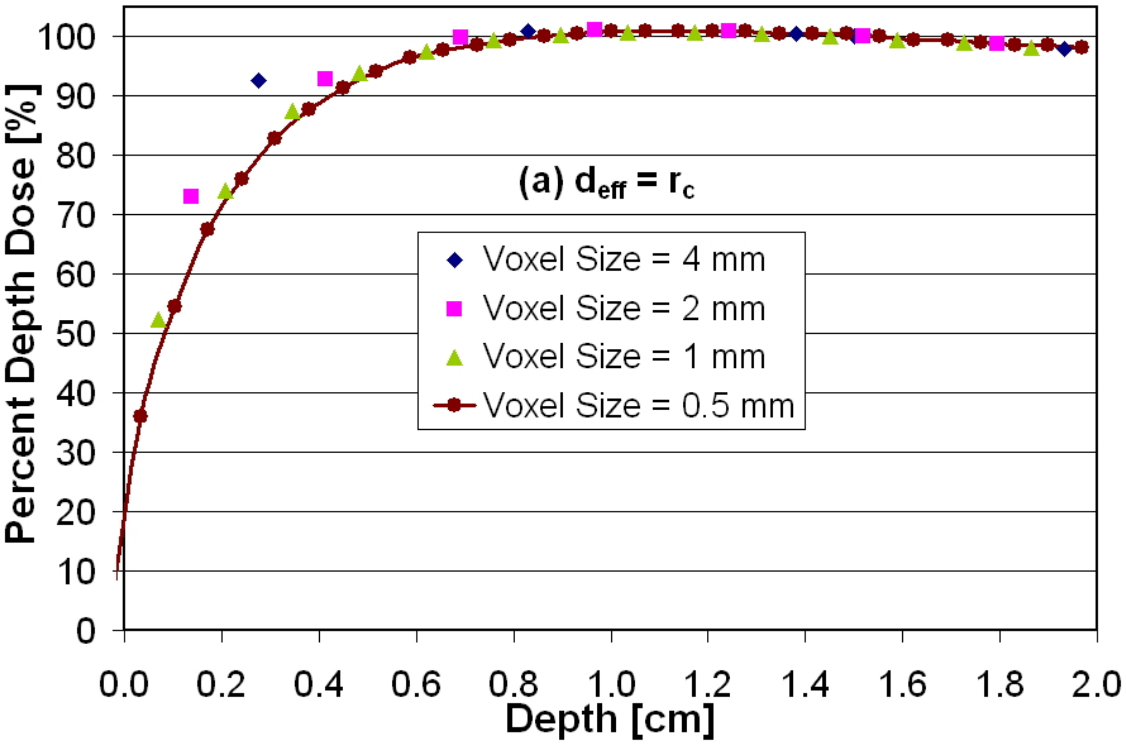

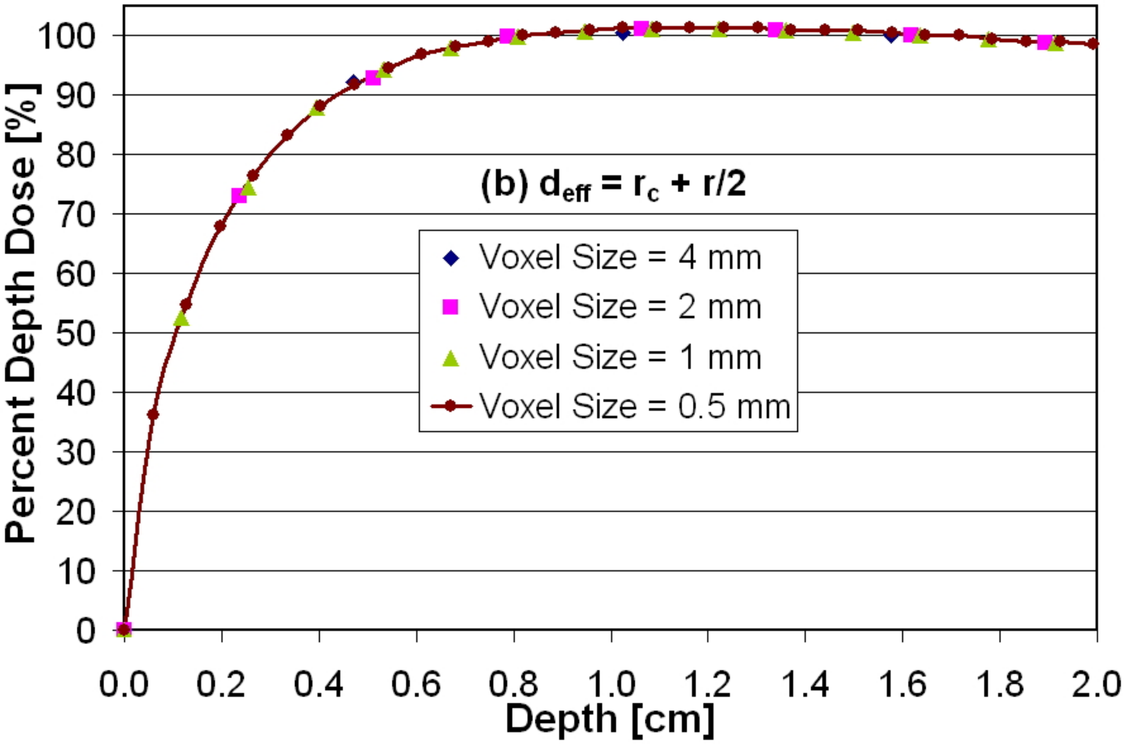

Figure 21. Percent depth dose plots from a 40x5 cm^2 beam at 45° angle of incidence showing calculated data that is plotted at an effective depth of (a) r_c and (b) $r_c + r/2$, where r is the voxel size.

Figure 21 (a) displays percent depth-dose plotted against depth along the central axis of the beam. The data are plotted for each of the dose grid resolutions described above. The first dose point is taken as the dose at an effective depth equal to r_c. There is disagreement in the data in Figure 21 (a) even though each dataset represents the same calculation parameters. Figure 21 (b) displays the same data, with the depth shifted by half a voxel length to account for the TERMA grid shift. The effective central axis depth is r_c plus r/2. As evident in Figure 21 (b), the data now show the same results for the same simulation condition. Thus, in this study, the calculated depth dose plots were shifted accordingly for the obliquely incident data.

2. Data Extraction

The EOP dose matrix was read and depth dose data were extracted from the center slice dose distribution. For the normally incident phantoms, data was extracted along the central axis of the beam from the surface to approximately 2.5 cm within the phantom. For the obliquely incident phantom plans, only one data point was extracted from the dose distribution for each phantom plan, along the central axis of the beam. This data point was located at the center of the point of measurement, at the entrance surface of the parallel-plate chamber. The same dose point was used for subsequent oblique-phantom plans, with depth added above the point of measurement.

Chapter 3: Results and Discussion

I. Aim 1

A. Normal Incidence Measurements

Data from the normal incidence measurements are plotted in Figure 22 as percent depth dose versus depth. Displayed are the measured profiles for static 40x5 cm^2 and 40x2.5 cm^2 beams at various SSDs (85, 70 and 55 cm). Data were normalized to a reference depth of 1.5 cm. The average fractional standard deviation of the mean for percent depth dose measurements was 0.3%. This uncertainty is small and is not plotted in Figure 22.

Dose measured at the surface varied weakly with SSD, increasing from 16.7% to 18.9% as the SSD decreased from 85 to 55 cm for the 40x5 cm^2 field. Dose measured at the surface increased from 12.7% to 14.9% as the SSD decreased from 85 to 55 cm for the 40x2.5 cm^2 field. Percent depth dose, however, increased rapidly with depth, reaching 90% of the dose at 1.5 cm at depths < 0.6 cm for all SSDs investigated and both field sizes. Surface doses were lower for the 40x2.5 cm^2 field because fewer contaminant electrons scatter into the field with a smaller field size (c.f., Chapter 1, Section B.2.a).

Percent depth dose in the buildup region measured at 55 cm SSD was a few percent greater than that measured at 70 and 85 cm SSD for both the 40x5 cm^2 and the 40x2.5 cm^2 field. This could be due to fewer contaminant electrons scattering out of the field when the phantom is closer to the source (55 cm SSD) than when the phantom is further from the source (70 and 85 cm SSD).

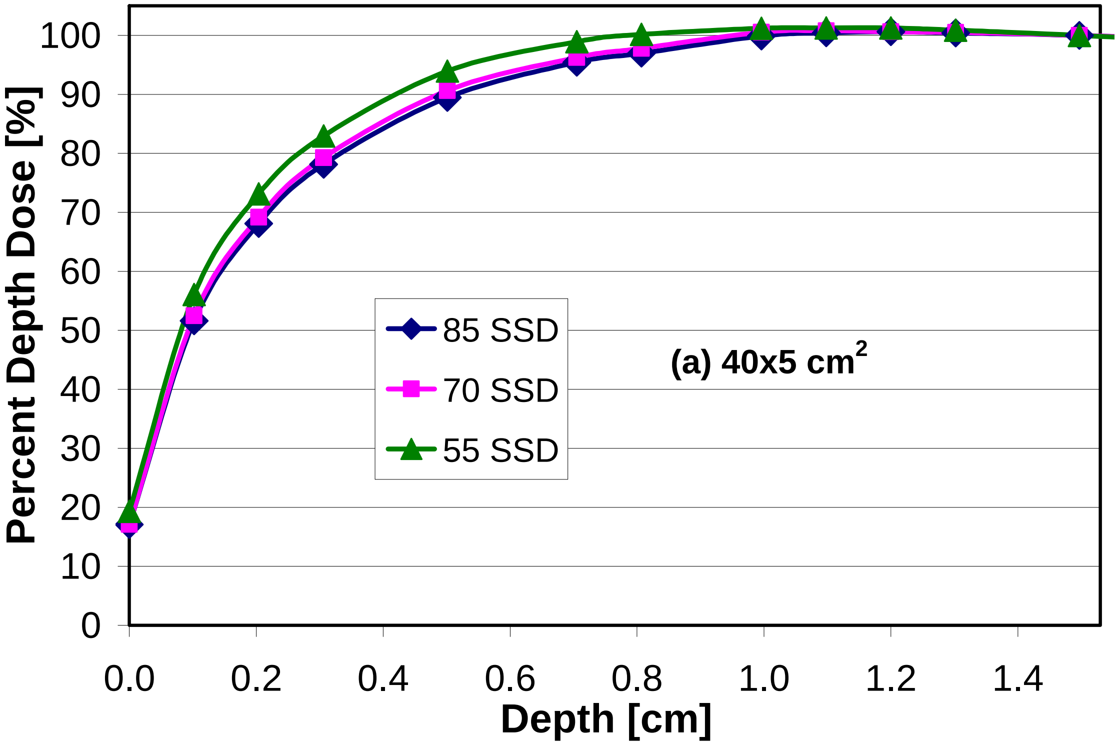

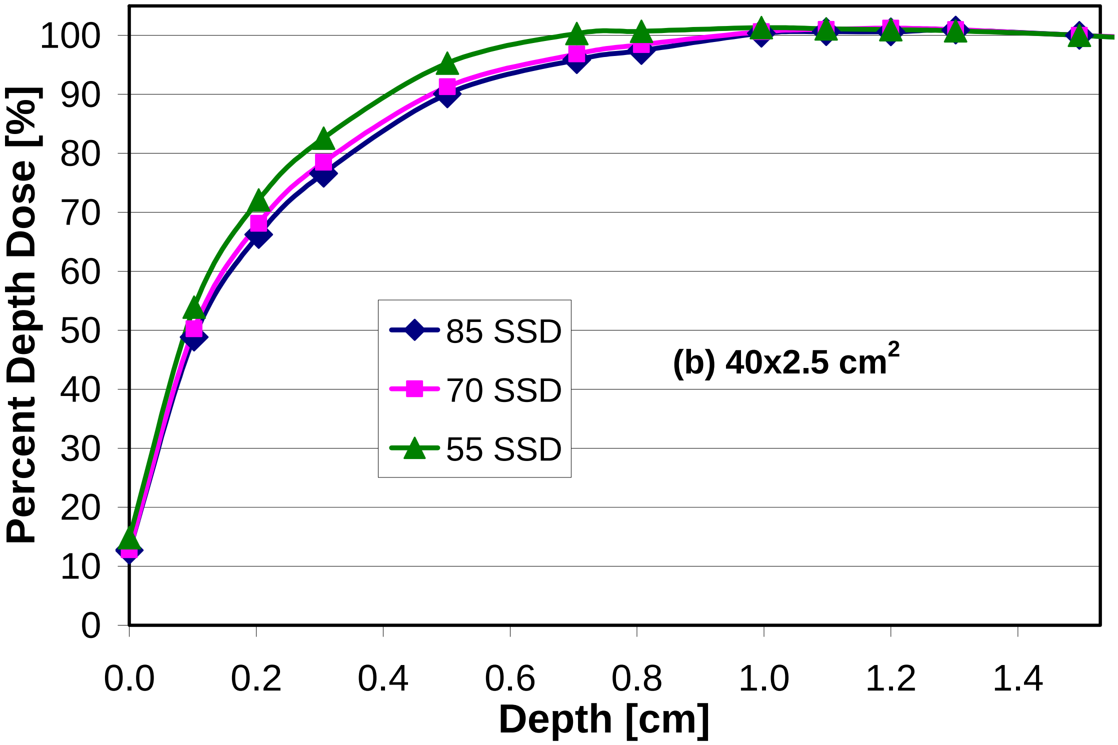

Figure 22. Percent depth dose plots at 85, 70 and 55 cm SSD for static (a) 40x5 cm^2 and (b) 40x2.5 cm^2 TomoTherapy beams. Data were normalized to a reference depth of 1.5 cm.

B. Oblique Incidence Measurements

Data from the oblique incidence measurements are plotted in Figure 24 as percent depth dose versus depth perpendicular to the surface of the phantom. Figure 23 illustrates the depth that is plotted. Displayed are the measured percent depth dose profiles for static 40x5 cm^2 and 40x2.5 cm^2 beams at various angles of incidence (0˚, 30˚, 45˚, 60˚, 75˚ and 83˚). Data were normalized to a reference depth of 1.5 cm of the normally incident (0˚) beam. The average fractional standard deviation of the mean for percent depth dose measurements was again small (0.3%) and is not plotted in Figure 24.

Dose measured at the surface varied significantly with increasing angle of incidence, increasing from 16.8% to 44.2% as the angle of incidence increased from 0˚ to 83˚ for the 40x5 cm^2 field. Dose measured at the surface increased from 12.8% to 42.6% as the angle of incidence increased from 0˚ to 83˚for the 40x2.5 cm^2 field. The increase in surface dose with increasing angle of incidence is likely a result of more forwardly scattered electrons in the phantom scattering to the surface (Gerbi et al., 1987).

As can be seen in Figure 24, the dose at the depth of maximum dose (d_{max}) decreased for increasing angle of incidence. This is an expected result of the increase in the central axis depth. As the beam angle increases, the distance along the central axis to a particular (perpendicular) depth increases as a function of the angle of incidence, as illustrated in Figure 23. In fact, this distance increases more rapidly for the higher oblique angles. For instance, when measuring the dose at a perpendicular depth of 2 cm for 75˚, the central axis depth is 7.7 cm (2 cm/cos75˚).

It can also be noted that d_{max} shifted toward a more shallow depth with increasing angle of incidence for both field sizes measured. For the 0˚ beam, d_{max} was approximately 1.5 cm for the 40x5 cm^2 field and 1.3 cm for the 40x2.5 cm^2 field. For the 30˚ beam, d_{max} was approximately 1.2 cm for the 40x5 cm^2 field and 1.0 cm for the 40x2.5 cm^2 field. For the 45° beam, d_{max} was approximately 1.1 cm for the 40x5 cm^2 field and 1.0 cm for the 40x2.5 cm^2 field. For the 60° beam, d_{max} was approximately 1.0 cm for the 40x5 cm^2 field and 0.8 cm for the 40x2.5 cm^2 field. For the 75° beam, d_{max} was approximately 0.5 cm for both the 40x5 cm^2 field and 40x2.5 cm^2 field. For the 83° beam, d_{max} was approximately 0.3 cm for both the 40x5 cm^2 field and the 40x2.5 cm^2 field. This is also an expected result since dose reaches its maximum value faster at oblique angles than at normal incidence again because of the increase in depth along the central axis.

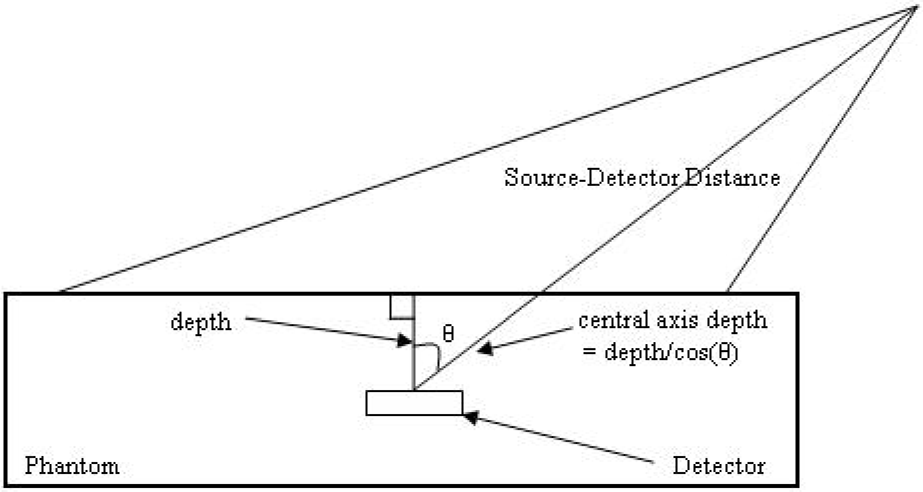

Figure 23. Illustration of the geometry of the plotted depth (perpendicular depth) and the central axis depth.

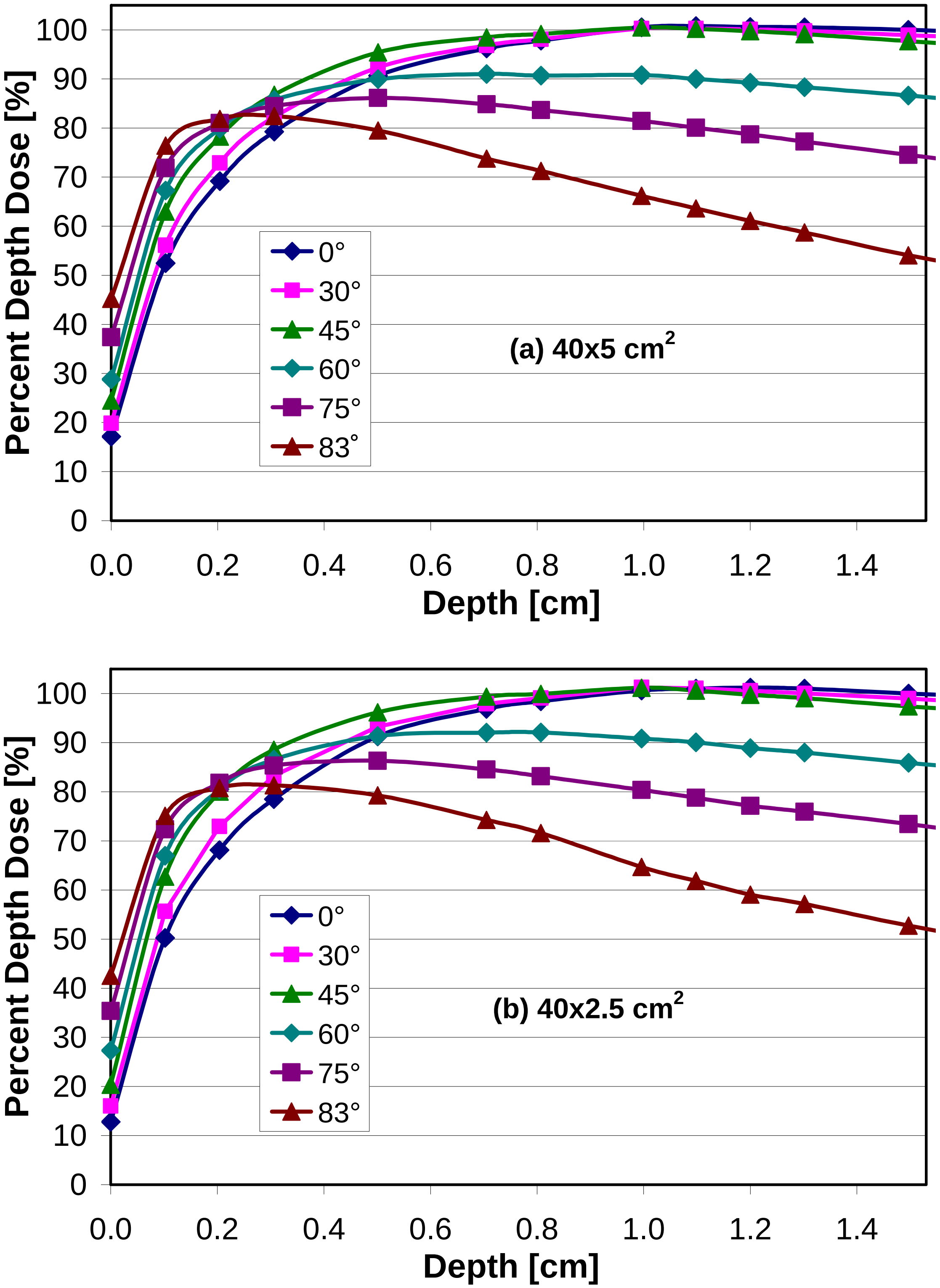

Figure 24. Percent depth dose plots at 70 cm SSD for various angles of incidence (0˚, 30˚, 45˚, 60˚, 75˚ and 83˚) for static (a) 40x5 cm^2 and (b) 40x2.5 cm^2 TomoTherapy beams. Plotted depth is the depth perpendicular to the surface of the phantom. Data were normalized to a reference depth of 1.5 cm of the 0˚ beam.

II. Aim 2

A. TLD Measurements

Results from the TLD measurements are shown in Figures 25 and 26. Data comparing the Attix chamber measurements to TLD measurements for a 40x5 cm^2 field at 0˚, 75˚, and 83˚ are shown in Figure 25. TLD measurements were made at depths < 0.5 cm and a depth of 1.5 cm. Data comparing measurements for a 40x2.5 cm^2 field at 60˚, 75˚, and 83˚ are shown in Figure 26. TLD measurements were only made at a depth of 1.5 cm for the 40x2.5 cm^2 field.

Both sets of measurements (Attix parallel-plate chamber and TLDs) are plotted as dose output [cGy/MU] versus depth perpendicular to the surface of the phantom. The average fractional standard deviation of the mean for measurements made with TLDs was 1.7%. This uncertainty is plotted with dose output in Figures 25 and 26. The average fractional standard deviation of the mean for measurements made with the Attix chamber was small (0.2%) and is not shown in Figures 25 and 26.

The TLD data agreed well with the Attix chamber data at 0˚, 60˚, 75˚ and 83˚ for both the 40x5 cm^2 and 40x2.5 cm^2 fields and all depths measured. Differences between Attix chamber and TLD data were evaluated at the depth of the TLD data. The corresponding Attix chamber data was found by linear interpolation from the depths of the Attix chamber measurements. For all measurements made at depths > 0.1 cm, the Attix chamber data and TLD data agreed to within 3% of the maximum dose. The error between measurements made closer to the surface (< 0.1 cm) was larger. The data agreed at a depth of 0.02 cm to within 6% of the maximum dose for the 40x5 cm^2 field at 75˚ and to within 9% of the maximum dose for the 40x5 cm^2 field at 0˚ and 83˚.

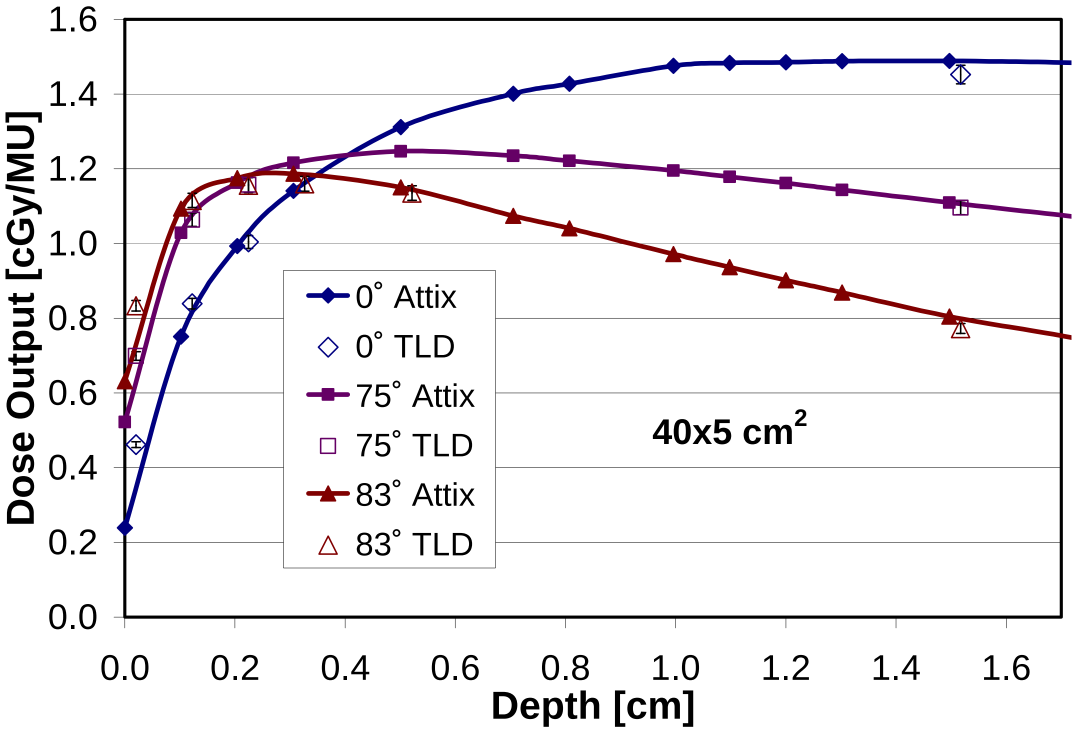

Figure 25. Comparison of measurements made with TLDs and the Attix parallel-plate chamber (Attix) for a 40x5 cm^2 beam at 0˚, 75˚ and 83˚ angle of incidence.

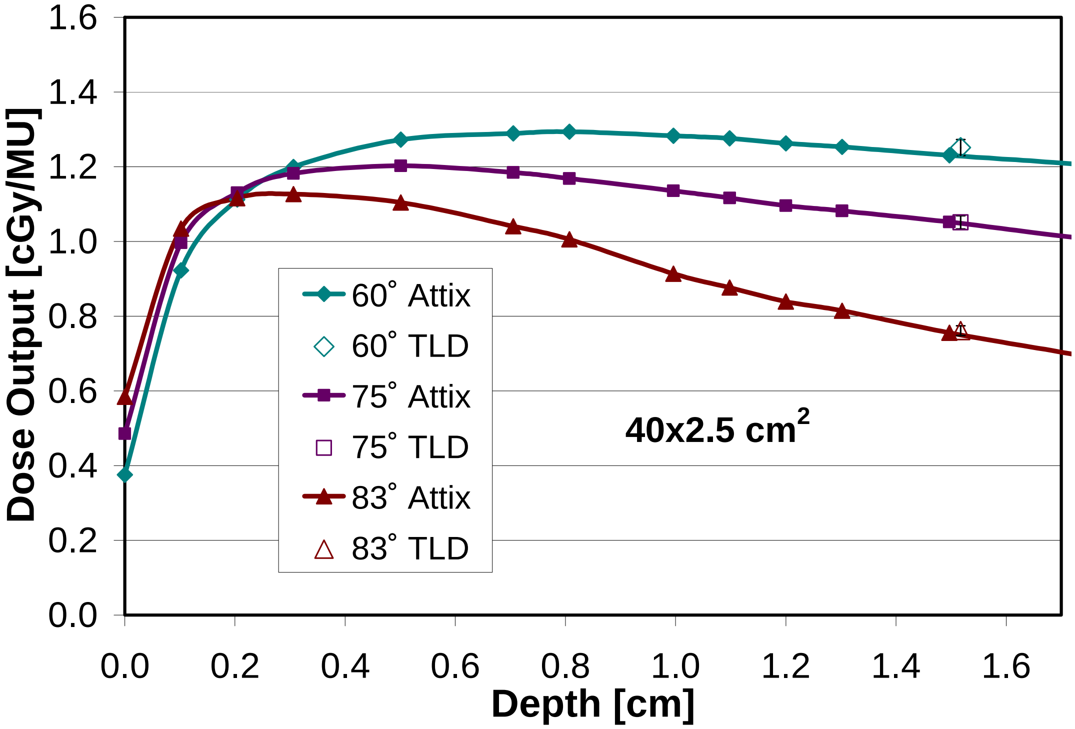

Figure 26. Comparison of measurements made with TLDs and the Attix parallel-plate chamber (Attix) for a 40x2.5 cm^2 beam at 60˚, 75˚ and 83˚ angle of incidence.

III. Aim 3

A. Normally Incident Beams

Plots comparing measured and calculated dose output [cGy/MU] versus depth for 40x5 cm^2 and 40x2.5 cm^2 normally incidence beams are shown in Figures 27-32. The average fractional standard deviation of the mean for measured dose output was small (0.2%) and is not shown in the plots. Differences between measured and calculated data were evaluated at the depths of the measured data. The corresponding calculated data was found by linear interpolation from the calculated data points.

The measured data were obtained at a constant SCD while adding depth, but the calculated data were extracted from the surface (at a constant SSD) to a depth of 2 cm. For the purposes of comparison, the calculated data were multiplied by an inverse square correction so that both sets of data are displayed as if the point of interest is at a constant distance from the source.

The calculated data were shifted in depth as described in Chapter 2, Section III.C.1. The first dose point in the calculated data exists within the first voxel of the simulated phantom. A point prior to this exists in air where the reported dose is set to 0.0 Gy. When appropriately shifted, the point in air is now representing a point at the surface of the phantom. Thus, the dose reported at the surface of the phantom is 0.0 Gy.

Figures 27 and 28 compare measured and calculated profiles for 85 cm source to detector distance, 0˚ angle of incidence for the 40x5 cm^2 and 40x2.5 cm^2 fields, respectively. Results show that the planning system's calculated dose: (1) under predicted the measured dose at the surface by 16.1% for the 40x5 cm^2 field and 12.2% for the 40x2.5 cm^2 field; (2) under predicted the measured dose at a depth of 0.1 cm by 9.3% for the 40x5 cm^2 field and 6.3% for the 40x2.5

cm^2 field; (3) over predicted the measured dose between depths of 0.5 cm and 1 cm by 3-4% for both field sizes and (4) agreed within 2% with measured doses at a depth of 1 cm and beyond for both field sizes.

Figures 29 and 30 compare measured and calculated profiles for 70 cm source to detector distance, 0° angle of incidence for the 40x5 cm^2 and 40x2.5 cm^2 fields, respectively. Results show that the planning system's calculated dose: (1) under predicted the measured dose at the surface by 16.1% for the 40x5 cm^2 field and 12.2% for the 40x2.5 cm^2 field; (2) under predicted the measured dose at a depth of 0.1 cm by 10.5% for the 40x5 cm^2 and 7.4% for the 40x2.5 cm^2 field and (3) agreed within 3% with measured doses at a depth of 0.3 cm and beyond for both field sizes.

Figures 31 and 32 compare measured to calculated profiles for 55 cm source to detector distance, 0° angle of incidence for the 40x5 cm^2 and 40x2.5 cm^2 fields, respectively. Results show that the planning system's calculated dose: (1) under predicted the measured dose at the surface by 17.9% for the 40x5 cm^2 field and 14.1% for the 40x2.5 cm^2 field; (2) under predicted the measured dose at depths of 0.1 cm and 0.2 cm by 7% or more for both field sizes and (3) agreed within 3% with measured doses at a depth of 0.5 cm and beyond for both field sizes.

All of the normally incident measurement conditions have a disagreement between measured and calculated data at the surface and superficial depths (depths ≤ 0.2 cm) where the planning system under predicted the dose. The planning system does not include an electron contamination dose, and this is likely the reason for the disagreement at superficial depths for all normally incident measurement conditions. The percent difference is highest at the surface and decreases with depth due to the short range of low energy contaminant electrons.

The disagreement at superficial depths is similar for 85 and 70 cm source to detector distance but increases for 55 cm source to detector. At a depth of 0.1 cm for the 40x5 cm^2 field, the planning system under predicts the dose by 9.3% for 85 cm source to detector, 10.5% for 70 cm source to detector and 15.7% for 55 cm source to detector. The measured data indicates that PDD increases slightly for 55 cm SSD at depths < 1 cm (c.f., Figure 22), and it is likely that this is due to electron contamination. As the SSD increases, there is more scattering of the contaminant electrons away from the narrow field, which would decrease the surface dose, improving agreement between measured and calculated dose at 70 and 85 cm SSD.

The measured data is consistently lower than the planning system's calculated data for the 40x2.5 cm^2 field for the normally incident measurement conditions. It was assumed that the cylindrical chamber was irradiated with a uniform dose and that the chamber exhibited a uniform response across the collecting volume. It is possible, however, that there was a slight volume effect with the cylindrical chamber for the 2.5 cm jaw. If the response was low for the cylindrical chamber, it would cause the Attix chamber data to be low as well.

B. Obliquely Incident Beams

Plots comparing measured and calculated dose output [cGy/MU] versus depth perpendicular to the surface of the phantom for 40x5 cm^2 and 40x2.5 cm^2 obliquely incident beams are shown in Figures 33-42.

Figures 33 and 34 compare measured and calculated profiles for 70 cm source to detector distance, 30° angle of incidence for the 40x5 cm^2 and 40x2.5 cm^2 fields, respectively. Results show that the planning system's calculated dose: (1) under predicted the measured dose at the surface by 18.8% for the 40x5 cm^2 field and 15.4% for the 40x2.5 cm^2 field; (2) under predicted the measured dose at a depth of 0.1 cm by 7.1% for the 40x5 cm^2 field and 5.5% for the 40x2.5

cm^2 field and (3) agreed within 3% with measured doses at a depth of 0.2 cm and beyond for both field sizes.

Figures 35 and 36 compare measured and calculated profiles for 70 cm source to detector distance, 45˚ angle of incidence for the 40x5 cm^2 and 40x2.5 cm^2 fields, respectively. Results show that the planning system's calculated dose: (1) under predicted the measured dose at the surface by 23.1% for the 40x5 cm^2 field and 19.5% for the 40x2.5 cm^2 field; (2) under predicted the measured dose at a depth of 0.1 cm by 7.0% for the 40x5 cm^2 field and 5.7% for the 40x2.5 cm^2 field and (3) agreed within 3% with measured doses at a depth of 0.2 cm and beyond for both field sizes.

Figures 37 and 38 compare measured to calculated profiles for 73 cm source to detector distance, 60˚ angle of incidence for the 40x5 cm^2 and 40x2.5 cm^2 fields, respectively. Results show that the planning system's calculated dose: (1) under predicted the measured dose at the surface by 30.2% for the 40x5 cm^2 field and 29.0% for the 40x2.5 cm^2 field and (2) agreed within 4% with measured doses at a depth of 0.1 cm and beyond for both field sizes.

Figures 39 and 40 compare measured to calculated profiles for 75 cm source to detector distance, 75˚ angle of incidence for the 40x5 cm^2 and 40x2.5 cm^2 fields, respectively. Results show that the planning system's calculated dose: (1) under predicted the measured dose at the surface by 41.9% for the 40x5 cm^2 field and 40.4% for the 40x2.5 cm^2 field; (2) agreed within 1% with measured doses at a depth of 0.1 cm for both field sizes; (3) over predicted the measured dose at depths of 0.2 cm and 0.3 cm by 3-4% for both field sizes and (4) agreed within 2% with measured doses at a depth of 0.5 cm and beyond for both field sizes.

Figures 41 and 42 compare measured to calculated profiles for 75 cm source to detector distance, 83˚ angle of incidence for the 40x5 cm^2 and 40x2.5 cm^2 fields, respectively. Results show that the planning system's calculated dose: (1) under predicted the measured dose at the surface by 53.2% for the 40x5 cm^2 field and 51.9% for the 40x2.5 cm^2 field; (2) over predicted the measured dose at a depth of 0.1 cm by 4.1% for the 40x5 cm^2 field and 6.9% for the 40x2.5 cm^2 field; (3) over predicted the measured dose at a depth of 0.2 cm by 3.0% for the 40x5 cm^2 field and 5.6% for the 40x2.5 cm^2 field and (4) agreed within 2% with measured doses at a depth of 0.5 cm and beyond for both field sizes.

All the obliquely incident measurement conditions have a disagreement between measured and calculated data at the surface. The lack of an electron contamination dose within the planning system contributes to this disagreement. More importantly, however, the surface dose increases with oblique incidence because more forward scattered electrons within the phantom are scattering to the surface. The disagreement between measured and calculated data at the surface increases with oblique incidence because the measured dose is increasing at the surface while planning system's calculated dose stays the same (0.0 Gy).

For the highly oblique measurement conditions (75˚ and 83˚), the planning system over predicted the measured dose between depths of 0.1 cm and 0.3 cm. This may be due to the failure of the convolution/superposition algorithm to account for reduced backscatter dose near the phantom/air interface. If this were the case, the effect would cause a larger disagreement with increasing angle of incidence and would decrease with depth. The data tend to support this hypothesis. For 75˚ angle of incidence (both field sizes) the planning system over predicted the dose between depths of 0.1 cm and 0.3 cm by as much as 3.5%. For 83˚ angle of incidence (both field sizes) the planning system over predicted the dose in this superficial region by as much as 6.9%. For both measurement conditions, the data agreed well at increasing depths, agreeing to within 2% at a depth of 0.5 cm and beyond.

For the oblique measurement conditions, the algorithm's lack of an electron contamination dose and the failure to account for the effect of missing material on the dose kernels (i.e., reduced backscatter) may tend to off-set each other. The lack of an electron contamination dose causes the planning system to under predict the dose at superficial depths and the failure to account for reduced scatter would causes the planning system to over predict the dose at superficial depths so that when these deficiencies are summed, they off-set each other. In fact, at the median angle measured (60˚), measured and calculated data agreed to within 4% for both field sizes between depths of 0.1 cm and 0.3 cm. For the other angles measured, the planning system either under predicted the dose at these depths by more than 4% (30˚ and 45˚) or over predicted the dose by more than 4% (83˚).

The measured data is again consistently lower than the planning system's calculated data for the 40x2.5 cm^2 field for the obliquely incident measurement conditions. This could be the result of a slight volume effect with the cylindrical chamber.

C. Summary of Results

A summary of the results comparing measured data with the Attix parallel-plate chamber to the treatment planning system's calculations is shown in Table 6 for the normally incident measurement conditions and in Table 7 for the obliquely incident measurement conditions. Differences between measured and calculated data were evaluated at the depths of the measured data. The corresponding calculated data was found by linear interpolation from the calculated data points. The percentage error reported is the difference between doses (calculated minus measured) as a percentage of the maximum dose of the measured data. The error at the surface is reported as well as the range of errors between a depth of 0.1 cm and d_{max} and the range of errors between a depth of d_{max} and 2.0 cm.

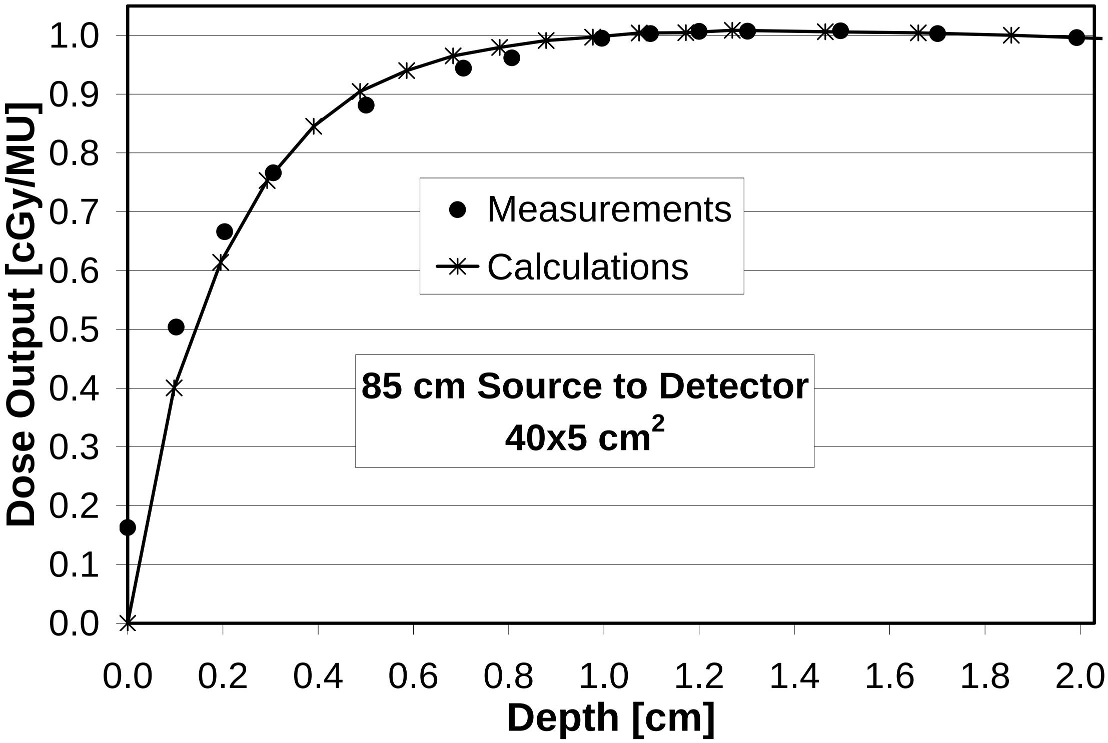

Figure 27. Comparison of measured to calculated data for a 40x5 cm^2 beam at 85 cm source to detector distance, 0˚ angle of incidence.

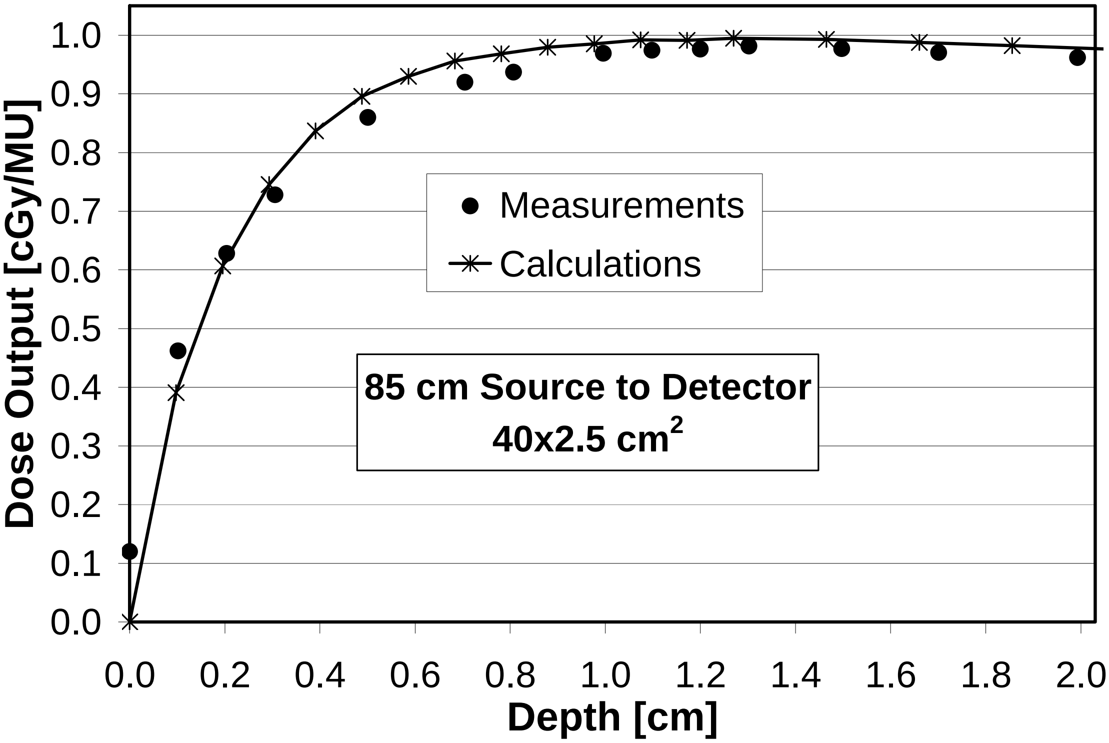

Figure 28. Comparison of measured to calculated data for a 40x2.5 cm^2 beam at 85 cm source to detector distance, 0˚ angle of incidence.

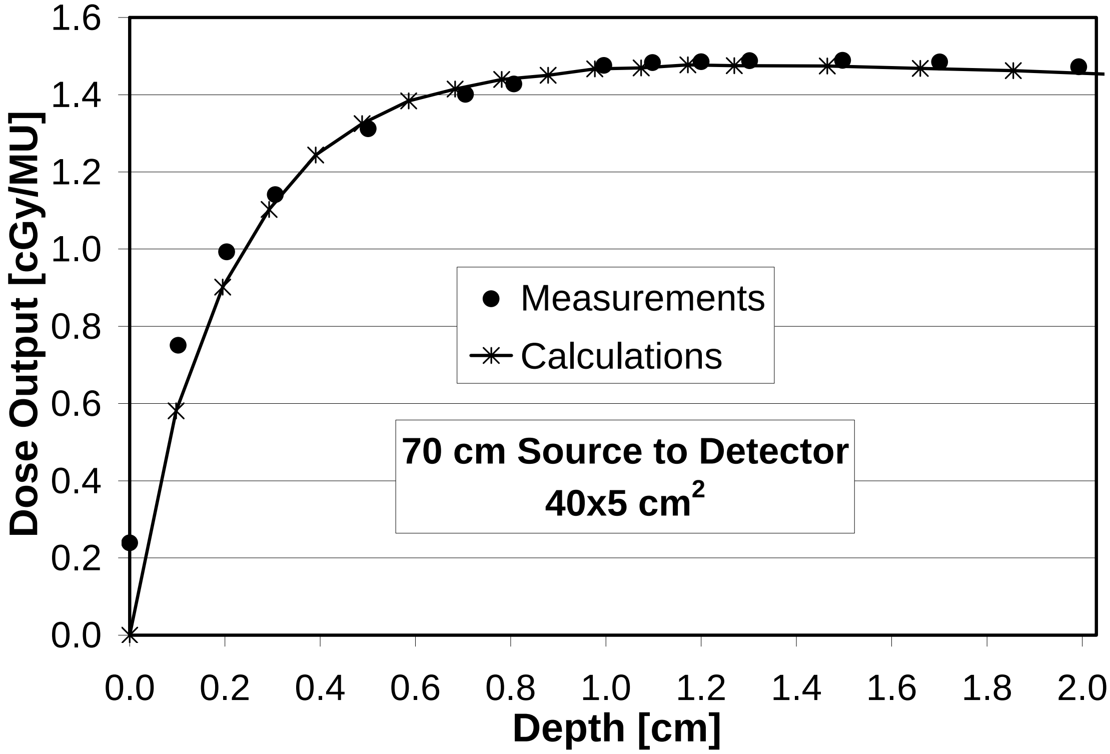

Figure 29. Comparison of measured to calculated data for a 40x5 cm^2 beam at 70 cm source to detector distance, 0° angle of incidence.

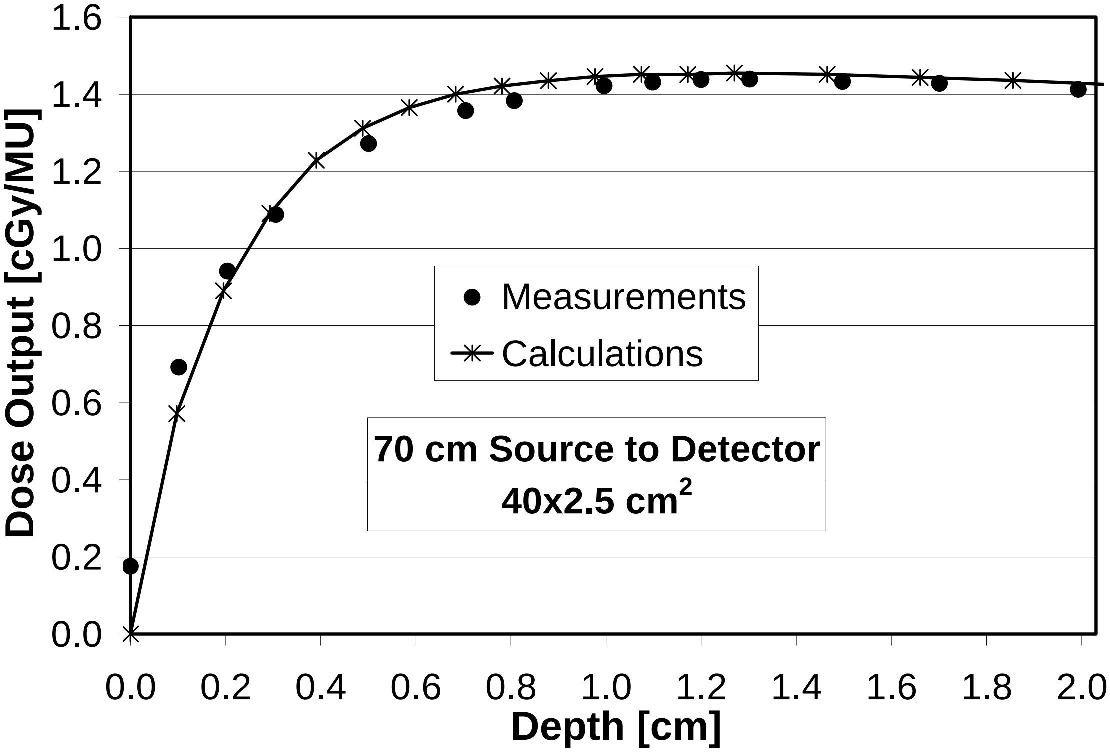

Figure 30. Comparison of measured to calculated data for a 40x2.5 cm^2 beam at 70 cm source to detector distance, 0° angle of incidence.

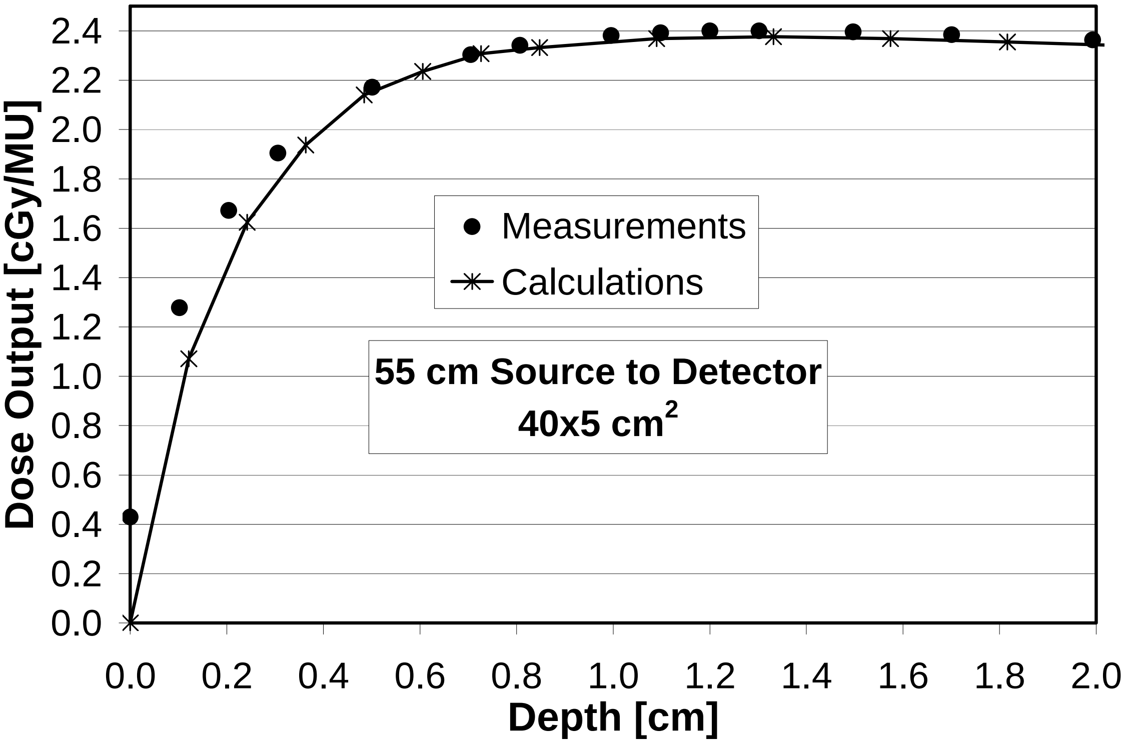

Figure 31. Comparison of measured to calculated data for a 40x5 cm^2 beam at 55 cm source to detector distance, 0˚ angle of incidence.

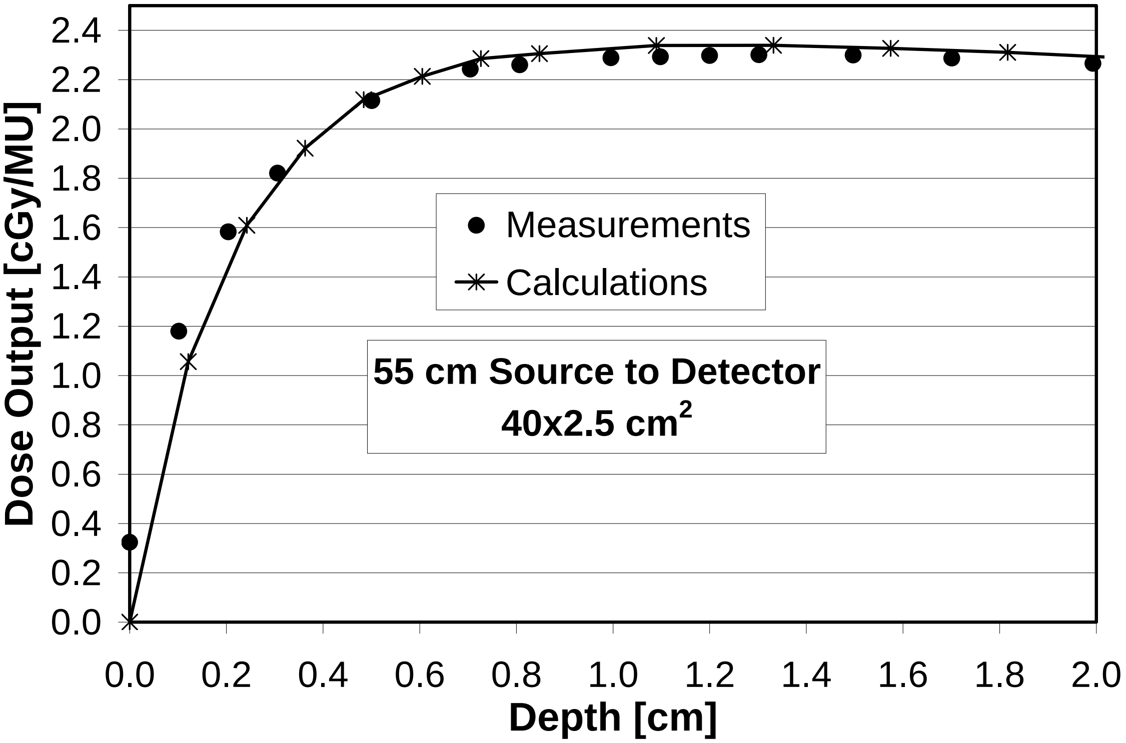

Figure 32. Comparison of measured to calculated data for a 40x2.5 cm^2 beam at 55 cm source to detector distance, 0˚ angle of incidence.

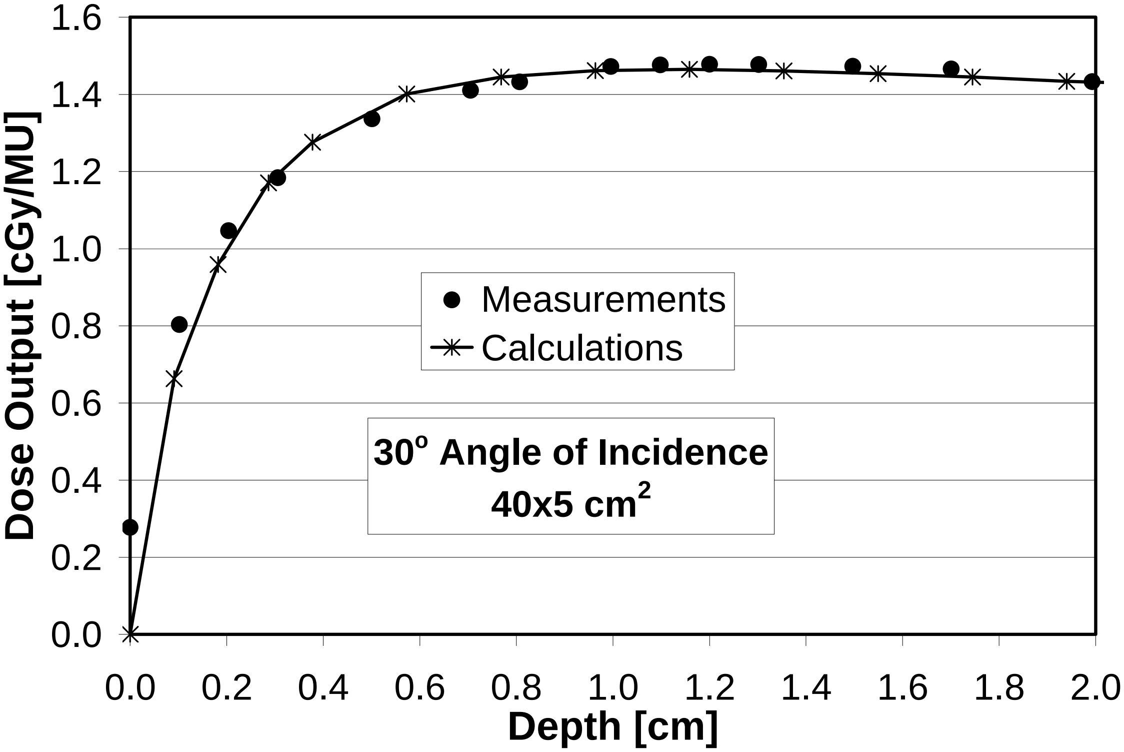

Figure 33. Comparison of measured to calculated data for a 40x5 cm^2 beam at 70 cm source to detector distance, 30˚ angle of incidence.

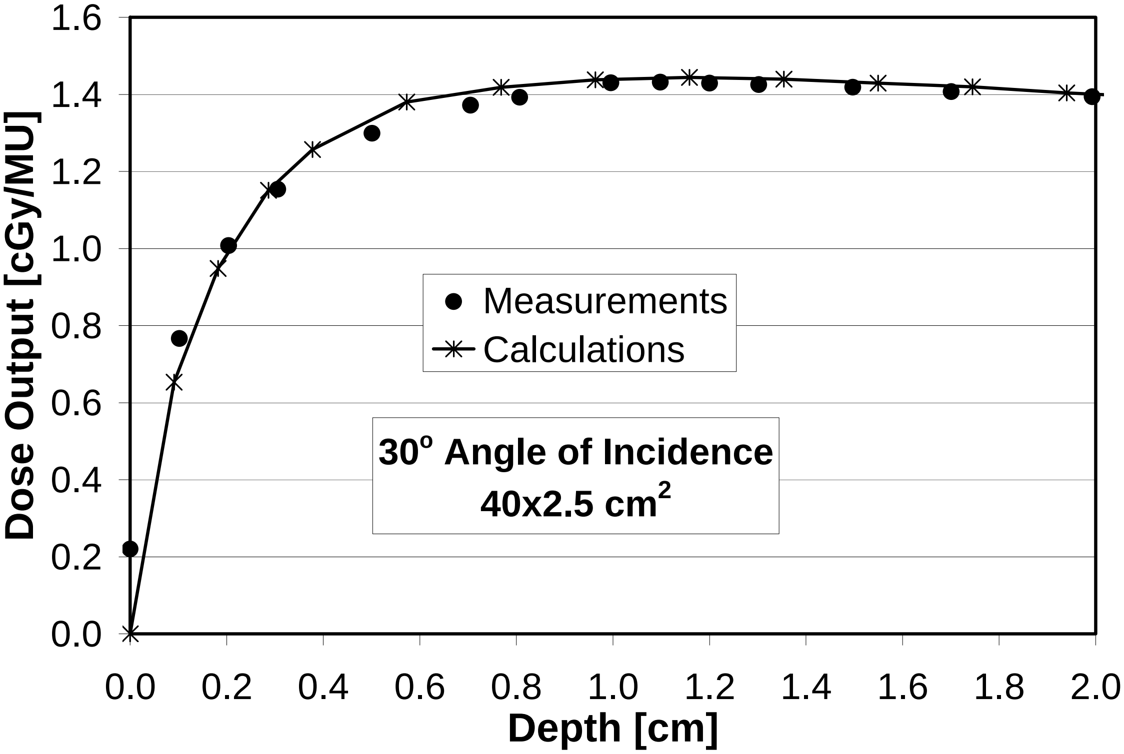

Figure 34. Comparison of measured to calculated data for a 40x2.5 cm^2 beam at 70 cm source to detector distance, 30˚ angle of incidence.

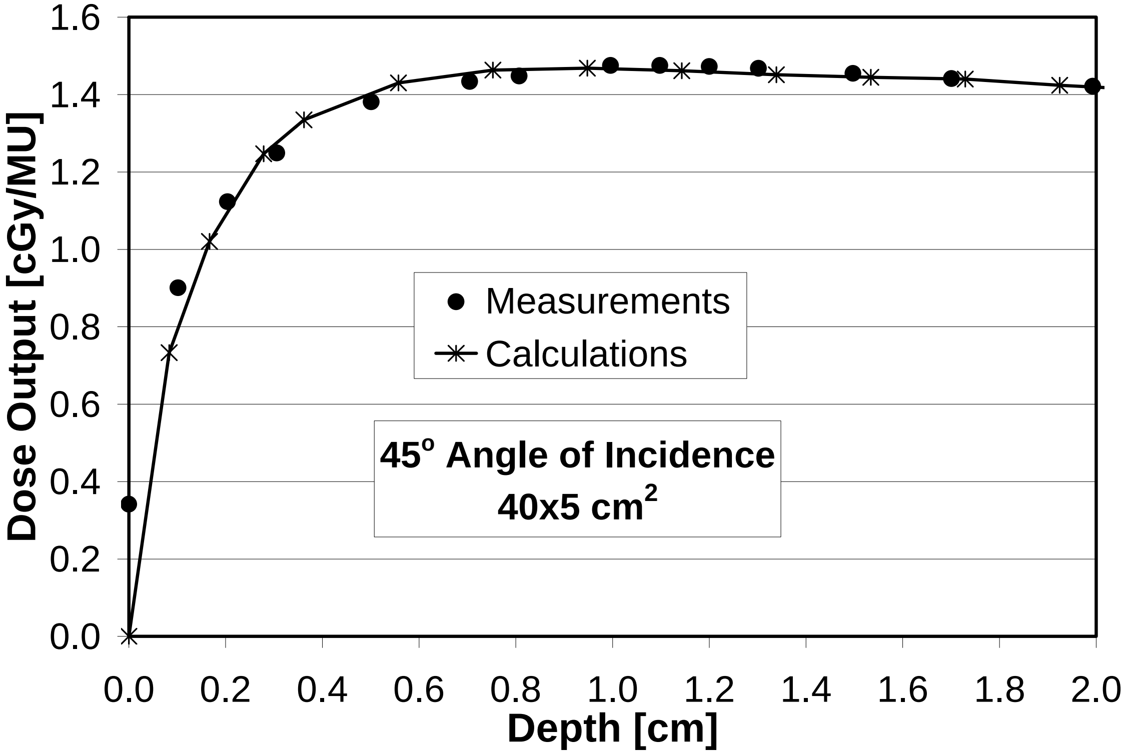

Figure 35. Comparison of measured to calculated data for a 40x5 cm^2 beam at 70 cm source to detector distance, 45˚ angle of incidence.

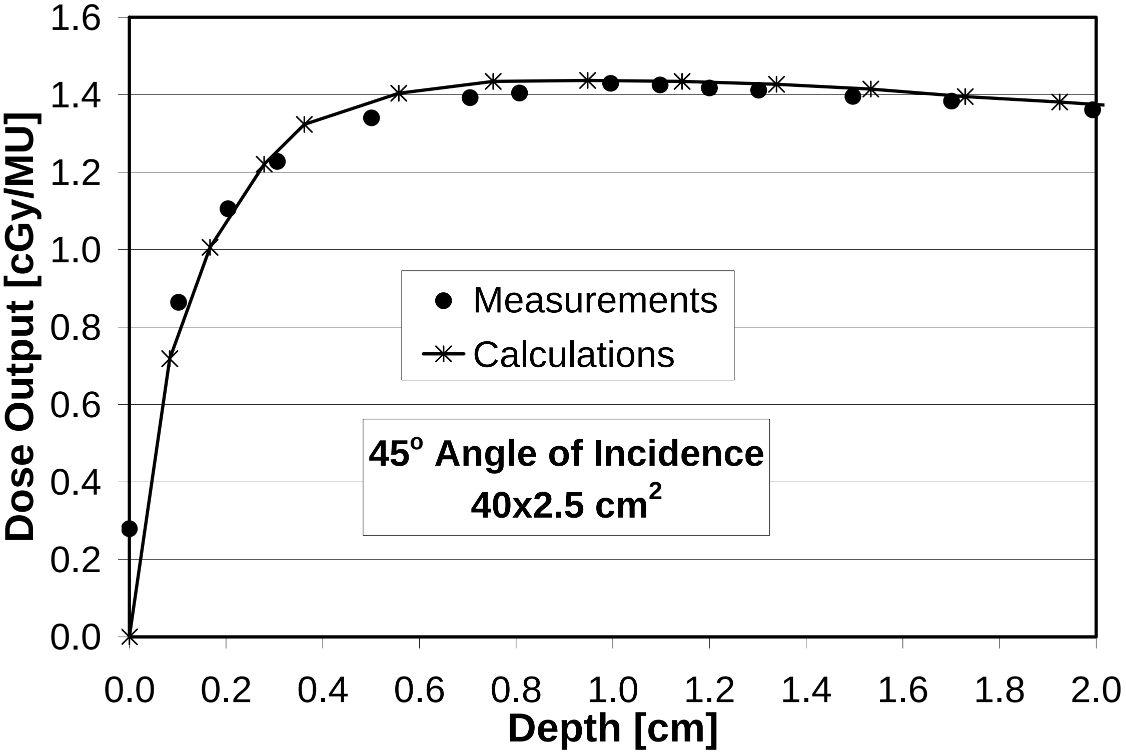

Figure 36. Comparison of measured to calculated data for a 40x2.5 cm^2 beam at 70 cm source to detector distance, 45˚ angle of incidence.

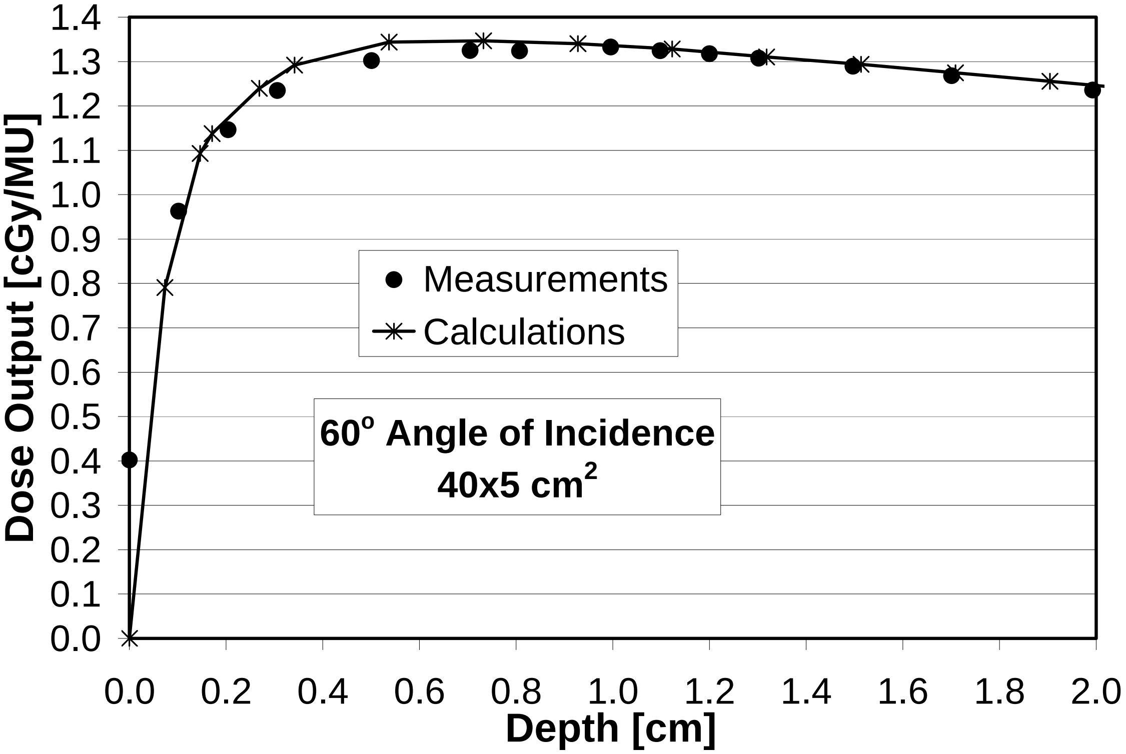

Figure 37. Comparison of measured to calculated data for a 40x5 cm^2 beam at 73 cm source to detector distance, 60˚ angle of incidence.

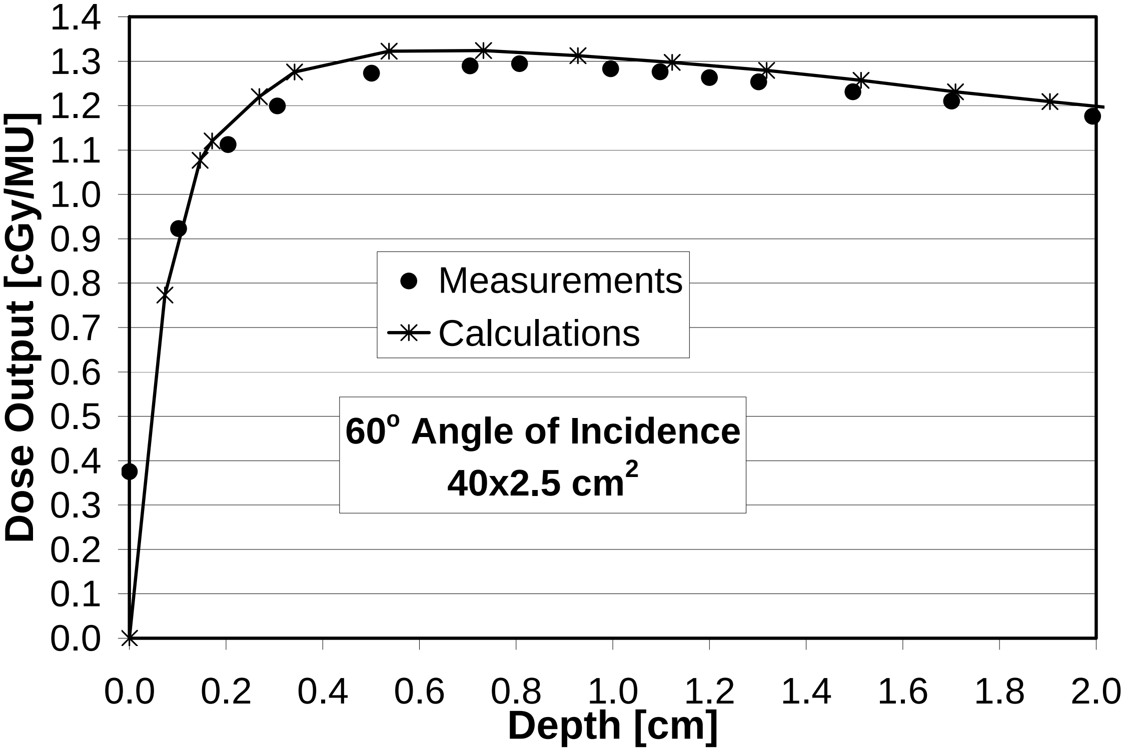

Figure 38. Comparison of measured to calculated data for a 40x2.5 cm^2 beam at 73 cm source to detector distance, 60˚ angle of incidence.

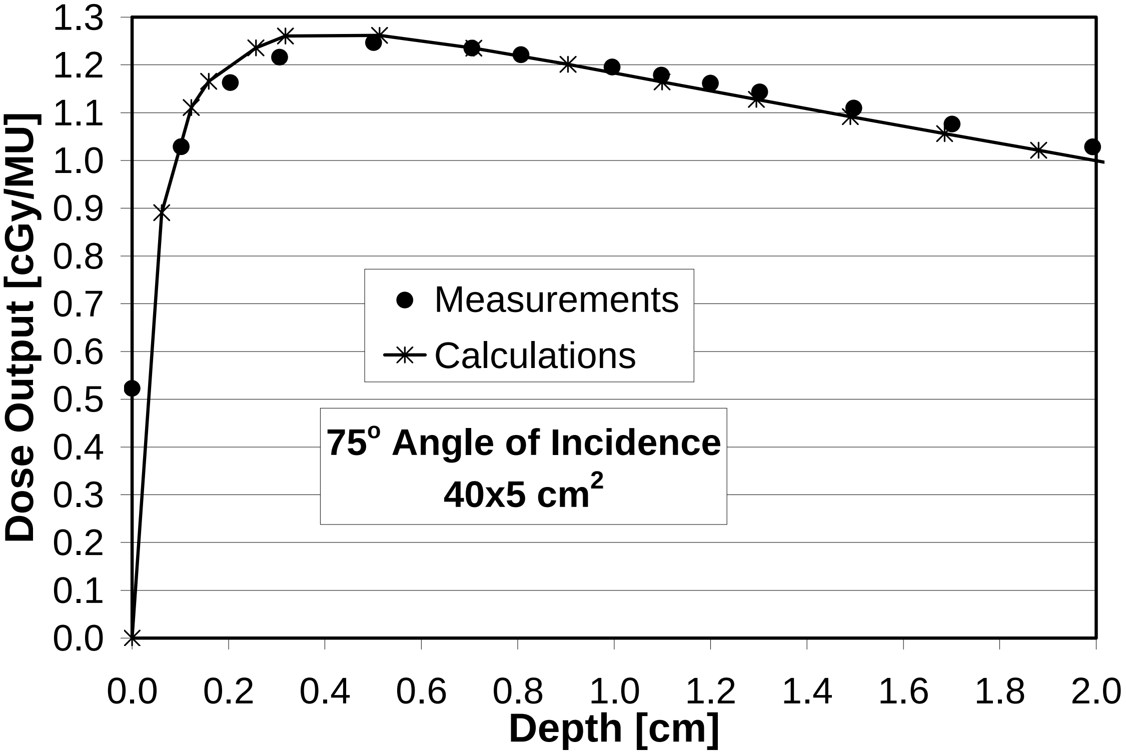

Figure 39. Comparison of measured to calculated data for a 40x5 cm^2 beam at 75 cm source to detector distance, 75˚ angle of incidence.

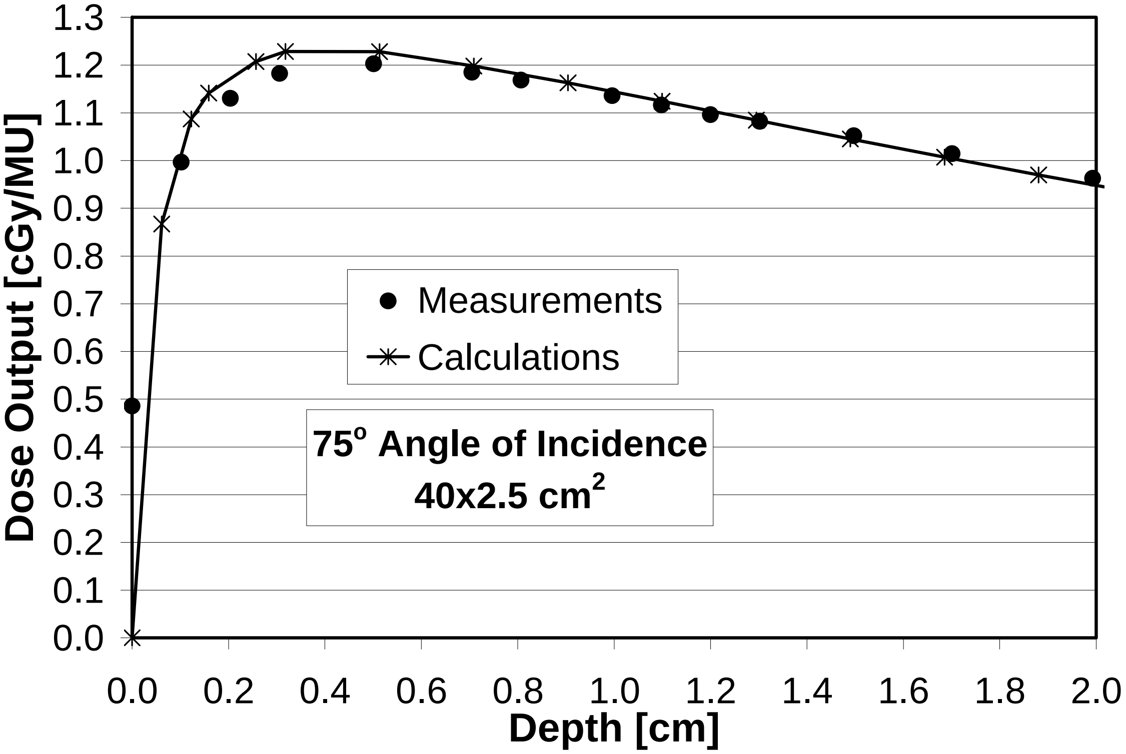

Figure 40. Comparison of measured to calculated data for a 40x2.5 cm^2 beam at 75 cm source to detector distance, 75˚ angle of incidence.

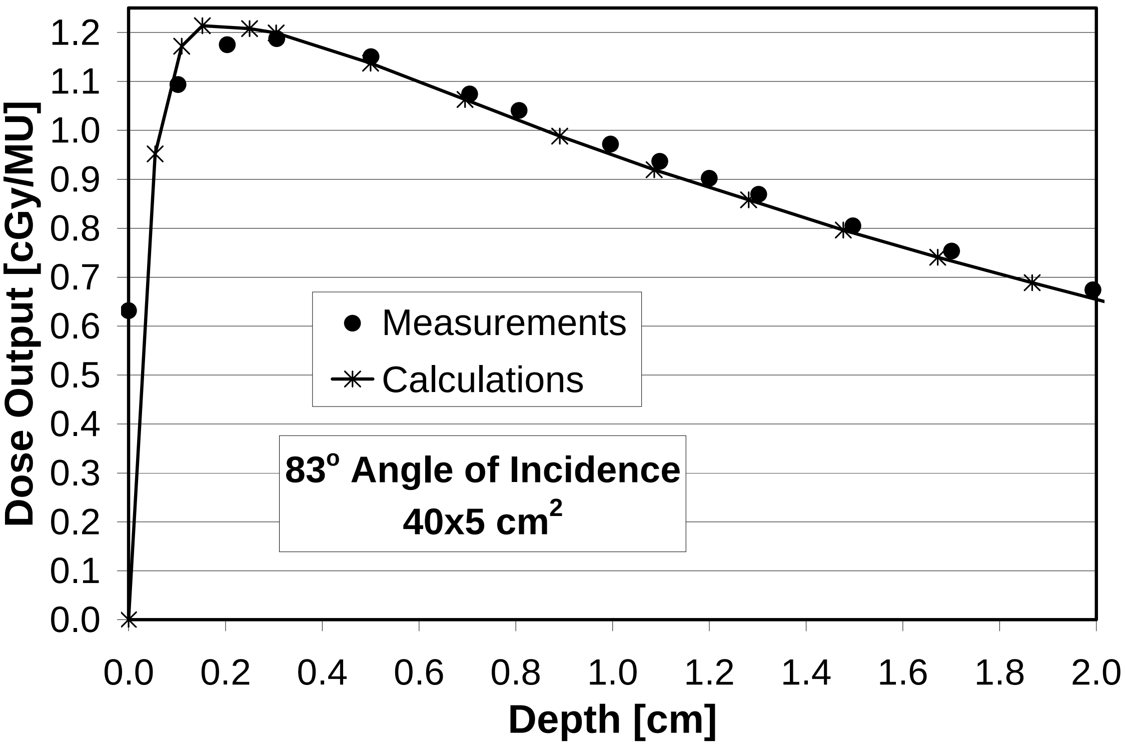

Figure 41. Comparison of measured to calculated data for a 40x5 cm^2 beam at 75 cm source to detector distance, 83˚ angle of incidence.

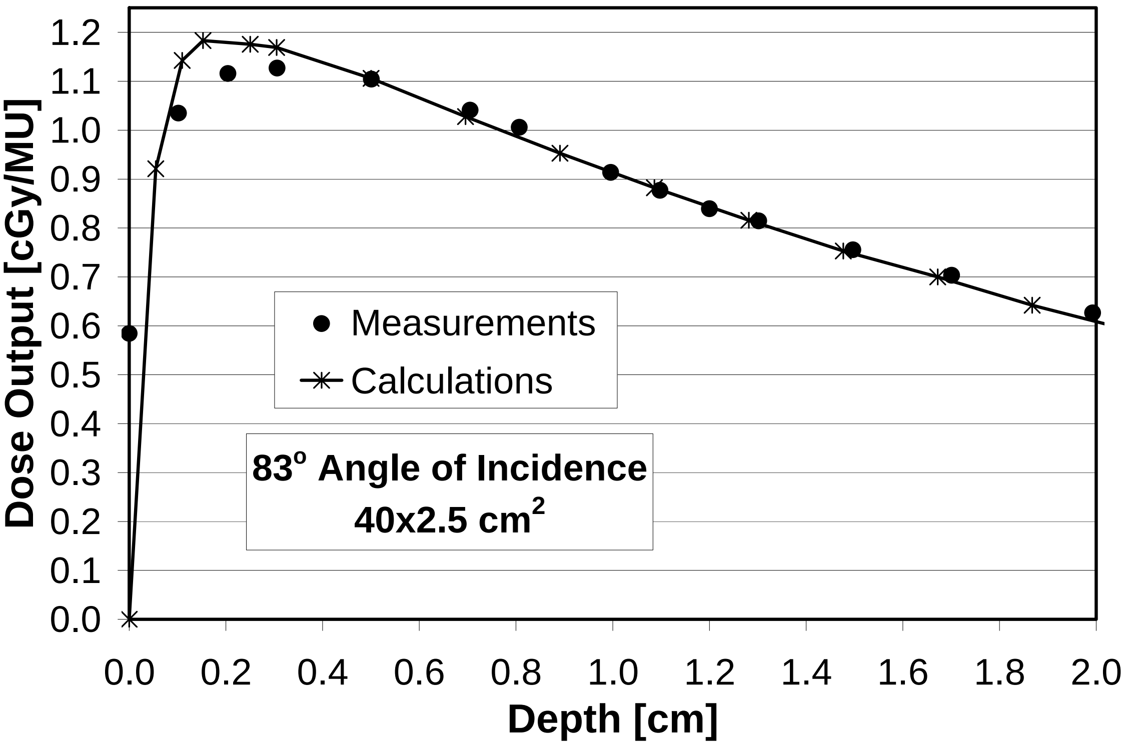

Figure 42. Comparison of measured to calculated data for a 40x2.5 cm^2 beam at 75 cm source to detector distance, 83˚ angle of incidence.

Table 6. The error between data (calculated minus measured) including the error at the surface, the range of errors between a depth of 0.1 cm and d_{max} and the range of errors between d_{max} and 2.0 cm for 40x5 cm^2 and 40x2.5 cm^2 normally incident TomoTherapy beams.

<table>
<tr><th colspan="4">40x5 cm^2</th></tr>
<tr><th>Measurement Condition</th><th>Error at Surface [%]</th><th>Range of Errors [%] (0.1 cm - d_{max})</th><th>Range of Errors [%] (d_{max} – 2.0 cm)</th></tr>
<tr><td>85 cm, 0 dg</td><td>-16.1</td><td>-9.3 to 2.8</td><td>-0.2 to 0.0</td></tr>
<tr><td>70 cm, 0 dg</td><td>-16.1</td><td>-10.5 to 1.3</td><td>-1.2 to -1.0</td></tr>
<tr><td>55 cm, 0 dg</td><td>-17.9</td><td>-15.7 to -0.2</td><td>-1.5 to -0.8</td></tr>
<tr><th colspan="4">40x2.5 cm^2</th></tr>
<tr><th>Measurement Condition</th><th>Error at Surface [%]</th><th>Range of Errors [%] (0.1 cm - d_{max})</th><th>Range of Errors [%] (d_{max} – 2.0 cm)</th></tr>
<tr><td>85 cm, 0 dg</td><td>-12.2</td><td>-6.3 to 4.1</td><td>1.3 to 1.7</td></tr>
<tr><td>70 cm, 0 dg</td><td>-12.1</td><td>-7.4 to 3.3</td><td>1.0 to 1.2</td></tr>
<tr><td>55 cm, 0 dg</td><td>-14.1</td><td>-12.6 to 2.6</td><td>0.6 to 1.6</td></tr>
</table>

Table 7. The error between data (calculated minus measured) including the error at the surface, the range of errors between a depth of 0.1 cm and d_{max} and the range of errors between d_{max} and 2.0 cm for 40x5 cm^2 and 40x2.5 cm^2 obliquely incident TomoTherapy beams.

<table>
<tr><th colspan="4">40x5 cm^2</th></tr>
<tr><th>Measurement Condition</th><th>Error at Surface [%]</th><th>Range of Errors [%] (0.1 cm - d_{max})</th><th>Range of Errors [%] (d_{max} – 2.0 cm)</th></tr>
<tr><td>70 cm, 30 dg</td><td>-18.8</td><td>-7.1 to 1.4</td><td>-1.3 to -0.1</td></tr>
<tr><td>70 cm, 45 dg</td><td>-23.1</td><td>-7.0 to 1.8</td><td>-0.9 to 0.0</td></tr>
<tr><td>73 cm, 60 dg</td><td>-30.2</td><td>-4.0 to 2.4</td><td>0.3 to 0.8</td></tr>
<tr><td>75 cm, 75 dg</td><td>-41.9</td><td>0.6 to 3.2</td><td>-2.2 to 1.2</td></tr>
<tr><td>75 cm, 83 dg</td><td>-51.9</td><td>3.0 to 4.1</td><td>-1.7 to 1.0</td></tr>
<tr><th colspan="4">40x2.5 cm^2</th></tr>
<tr><th>Measurement Condition</th><th>Error at Surface [%]</th><th>Range of Errors [%] (0.1 cm - d_{max})</th><th>Range of Errors [%] (d_{max} – 2.0 cm)</th></tr>
<tr><td>70 cm, 30 dg</td><td>-15.4</td><td>-5.5 to 2.5</td><td>0.5 to 1.0</td></tr>
<tr><td>70 cm, 45 dg</td><td>-19.5</td><td>-5.7 to 2.9</td><td>0.5 to 1.5</td></tr>
<tr><td>73 cm, 60 dg</td><td>-29.0</td><td>-2.3 to 3.8</td><td>1.7 to 2.2</td></tr>
<tr><td>75 cm, 75 dg</td><td>-40.4</td><td>1.3 to 3.5</td><td>-1.1 to 2.1</td></tr>
<tr><td>75 cm, 83 dg</td><td>-51.9</td><td>5.6 to 6.9</td><td>-1.9 to 3.7</td></tr>
</table>

Chapter 4: Conclusions and Recommendations

I. Conclusions

The hypothesis tested in this work was that superficial doses measured on the central axis from a static TomoTherapy beam agree with doses calculated by the TomoTherapy planning system to within 5% (of the maximum dose) for angles of incidence 0˚-83˚. This hypothesis is not true due to the following: (1) for all measurement conditions, the planning system under predicted the dose at the surface by more than 5% of the maximum dose; (2) for all normally incident measurement conditions, the planning system under predicted the dose at a depth of 0.1 cm by more than 5% of the maximum dose; (3) for 55 cm source to detector, the planning system under predicted the dose at a depth of 0.2 cm by more than 5% of the maximum dose; (4) for 30˚ and 45˚ angle of incidence, the planning system under predicted the dose at a depth of 0.1 cm by more than 5% of the maximum dose and (5) for 75˚ and 83˚ angle of incidence, the planning system over predicted the dose at superficial depths (0.1 cm to 0.3 cm) by as much as 7%. However, the results of this work support the hypothesis at depths ≥ 0.3 cm.

II. Clinical Impact and Clinical Recommendations

The results of this work indicate discrepancies between measured and calculated data at superficial depths (≤ 0.3 cm), and therefore, the use of bolus is recommended when treating lesions that lie within this range of depth. The thickness of the bolus material used should be at least 0.3 cm so that the entire lesion would be placed at a depth where the dose is accurately predicated by the treatment planning system.

III. Recommendations for the TomoTherapy Treatment Planning System

As a result of this work, deficiencies were noted in the TomoTherapy's dose calculation algorithm and recommendations can be made to improve the algorithm. First, the planning system does not currently model electron contamination. The addition of an electron contamination dose would impact the dose in the build-up region and improve agreement at the surface and superficial depths (depths ≤ 0.3 cm). Second, the TERMA grid points are offset from the center of the pixel. A shift in depth is required to correctly analyze depth dose data and clinically, the dose reported at the surface is not an accurate representation of the dose at the surface. Shifting the TERMA grid points to the center of the voxel would eliminate the need for a shift in depth dose data and give a more accurate representation of the dose at the surface of a patient. Third, the algorithm fails to account for the effect of missing material on the dose kernels and the reduction in backscatter at the phantom/air interface for oblique angle conditions. This causes the planning system to overestimate the dose at superficial depths for highly oblique incidence. Accounting for the reduced scatter may improve the agreement at superficial depths for highly oblique angles.

References

Abdel-Rahman, W., J.P. Seuntjens, F. Verhaegen, F. Deblois, E.B. Podgorsak. (2005). "Validation of Monte Carlo calculated surface doses for megavoltage photon beams." *Med. Phys.* 32:286-298.

Aird, E.G.A, J.E. Burns, M.J. Day, S. Duane, T.J. Jordan, A Kacperek, S.C. Klevenhagen, R.M. Harrison, S.C. Lillicrap, A.L. McKenzie, W.G. Pitchford, J.E. Shaw, C.W. Smith. (1996). *Central Axis Depth Dose Data for Use in Radiotherapy. British Journal of Radiology. Supplement 25.* British Institute of Radiology: London.

Almond, P.R., F.H. Attix, L.J. Humphries, H. Kubo, R. Nath, S. Goetsch, D.W.O. Rogers. (1994). "The calibration and use of plane-parallel ionization chambers for dosimetry of electron beams: An extension of the 1983 AAPM protocol report of AAPM Radiation Therapy Committee Task Group No. 39." *Med. Phys.* 21:1251-1260.

Almond, P.R., P.J. Biggs, B.M. Coursey, W.F. Hanson, M.S. Huq, R. Nath, D.W.O. Rogers. (1999). "AAPM's TG-51 protocol for clinical reference dosimetry of high energy photon and electron beams." *Med. Phys.* 26:1847-1870.

Ashenafi, M., R. Boyd, K. Lo, T. Lee, K. Hogstrom. (2006). "Comparison of TomoTherapy with Conventional Electron/X-Ray Treatment Plans for Chest Wall." *Med. Phys.* 33:2175.

Attix, F.H. (1993). "Application of a commercial solid water plane-parallel ionization chamber to the AAPM TG-21 protocol." *Med. Phys.* 20:735-737.

Balog, J.P., T.R. Mackie, P. Reckwerdt, M. Glass, L. Angelos. (1999). "Characterization of the output for helical delivery of intensity modulated slit beams." *Med. Phys.* 26:55-64.

Biggs, P.J., M.D. Russell. (1983). "An investigation into the presence of secondary electrons in megavoltage photon beams." *Phys. Med. Biol.* 28:1033-1043.

Cheek, D., K. Hogstrom, J. Gibbons, I. Rosen. (2006). "Utility of film dosimetry for assessing TomoTherapy treatments of superficial PTVs." *Med. Phys.* 33:2148.

Day, M.J., E.G.A. Aird. (1995). "The equivalent field method for dose determinations in rectangular fields." *British Journal of Radiology Supplement 25: Central Axis Depth Dose Data for Use in Radiotherapy*. 138-151. British Institute of Radiology: London.

Gerbi, B.J. (1993). "The response characteristics of a newly designed plane-parallel ionization chamber in high-energy photon and electron beams." *Med. Phys.* 20:1411-1415.

Gerbi, B.J., A.S. Meigooni, F.M. Kahn. (1987). "Dose buildup for obliquely incident photon beams." *Med. Phys.* 14:393-399.

Gerbi, B.J., F.M. Kahn. (1987). "The polarity effect for commercially available plane-parallel ionization chambers." *Med Phys.* 14:210-215.

Gerbi, B.J., F.M. Kahn. (1997). "Plane-parallel ionization chamber response in the buildup region of obliquely incident photon beams." *Med. Phys*. 24:873-878.

International Electrotechnical Commission, Report No. 61217 "Radiation equipment – coordinates, movements, scales." (2002).

Jeraj, R., T.R. Mackie, J. Balog, G. Olivera, D. Pearson, J. Kapatoes, K. Ruchala, P. Reckwerdt. (2004). "Radiation characteristics of helical tomotherapy." *Med. Phys.* 31:396-403.

Jursinic, P.A., T.R. Mackie. (1996). "Characteristics of secondary electrons produced by 6, 10, and 24 MV x-ray beams." *Phys. Med. Biol.* 41:1499-1509.

Khan, F.M. (2003). *The Physics of Radiation Therapy.* 3rd Ed. Lippincott Williams & Wilkins: Philadelphia. p. 282.

Kim, S., C.R. Liu, T.C. Zhu, J.R. Palta. (1998). "Photon beam skin dose analyses for different clinical setups." *Med. Phys.* 25:860-866.

Lamb, A., S. Blake. (1998). "Investigation and modeling of the surface dose from linear accelerator produced 6 and 10 MV photon beams." *Phys. Med. Biol.* 43:1133-1146.

Low, D.A., S. Mutic. (1998). "A commercial IMRT treatment-planning dose-calculation algorithm." *Int. J. Radiation Oncology Biol. Phys.* 41:933-937.

Lu, W., G.H. Olivera, M. Chen, P. Reckwerdt, T.R. Mackie. (2005). "Accurate convolution/superposition for multi-resolution dose calculation using cumulative tabulated kernels." *Phys. Med. Biol.* 50:655-680.

Mackie, T.R., J.W. Scrimger, J.J. Battista. (1985). "A convolution method of calculating dose for 15-MV x rays." Med. Phys. 12:188-196.

Mackie, T.R., A.F. Bielajew, D.W.O. Rogers, J.J. Battista. (1988). "Generation of photon energy deposition kernels using the EGS Monto Carlo code." *Phys. Med. Biol.* 33:1-20.

Mackie, T.R., T. Holmes, S. Swerdloff, P. Reckwerdt, J.O. Deasy, J. Yang, B. Paliwal, T. Kinsella. (1993). "Tomotherapy: A new concept for the delivery of dynamic conformal radiotherapy." *Med. Phys.* 20:1709-1719.

Mackie, T.R., H.H. Liu, E.C. McCullough, F.M. Kahn, ed., R.A. Potish, ed. (2000). "Treatment Planning Algorithms." *Treatment Planning in Radiation Oncology.* Lippincott Williams & Wilkins: Philidelphia.

Mackie, T.R., G.H. Olivera, J.M. Kapatoes, K.J. Ruchala, J.P. Balog, W.A. Tome, S. Hui, M. Kissick, C. Wu, R. Jeraj, P. Reckwerdt, P. Harari, M. Ritter, L. Forrest, J.S. Welsh, M.P. Mehta, J.R. Palta, ed. (2003). "Helical TomoTherapy." *Intensity-Modulated Radiation Therapy: The State of the Art.* 2003 AAPM Summer School Proceedings. Medical Physics Publising:Madison, WI.

Malataras, G., C. Kappas, D.M.J. Lovelock. (2001). "A Monte Carlo approach to electron contamination sources in the Saturne-25 and -41." *Phys. Med. Biol.* 46:2435-2446.

McKenzie, A.L., P.H. Stevens. (1993). "How is photon head scatter in a linear accelerator related to the concept of a virtual source?" *Phys. Med. Biol.* 38:1173-1180.

Mitchell, M.J., C. Ramsey. (2006). "Surface dose measurements for Intensity Modulated Radiation Therapy." *Med. Phys.* 33:2249.

Mutic, S., D.A. Low. (2000). "Superficial doses from serial tomotherapy delivery." *Med. Phys.* 27:163-165.

Orton, N., H. Jaradat, J. Welsh, W. Tome. (2005). "Total scalp irradiation using helical tomotherapy." *Medical Dosimetry.* 30:162-168.

Rawlinson, J.A., D. Arlen, D. Newcombe. (1992). "Design of parallel plate ion chambers for buildup measurements in megavoltage photon beams." *Med. Phys.* 19:641-648.

Schnarr, E., G.H. Olivera. (2006). Personal communication.

Tello, V.M., R.C. Tailor, W.F. Hanson. (1995). "How water equivalent are water-equivalent solid materials for output calibration of photon and electron beams?" Med. Phys. 22:1177-1189.

Tung, S.S., A.S. Shiu, G. Starkschall, W.H. Morrison, K.R. Hogstrom. (1993). "Dosimetric evaluation of total scalp irradiation using lateral electron-photon technique." *Int. J. Radiation Oncology Biol. Phys.* 27:153-160.

Yorke, E.D., C.C. Ling, S. Rustgi. (1985). "Air-generated electron contamination of 4 and 10 MV photon beams: comparison of theory and experiment." *Phys. Med. Biol.* 30:1305-1314.

Appendix: Calibration Curves for TLD Data

Calibration curves for the determination of dose with the TLD data are presented in the Appendix.

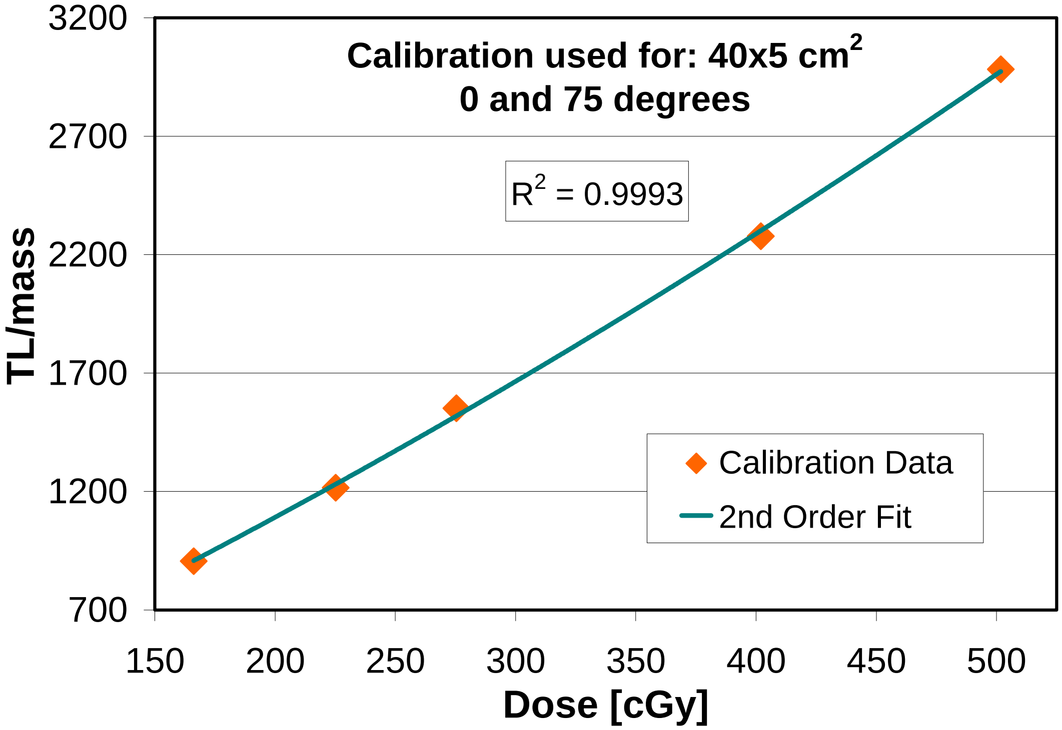

Figure 43. Calibration curve used for interpolating unknown doses measured with TLDs for the measurement of a 40x5 cm^2 beam at 0° and 75° angle of incidence.

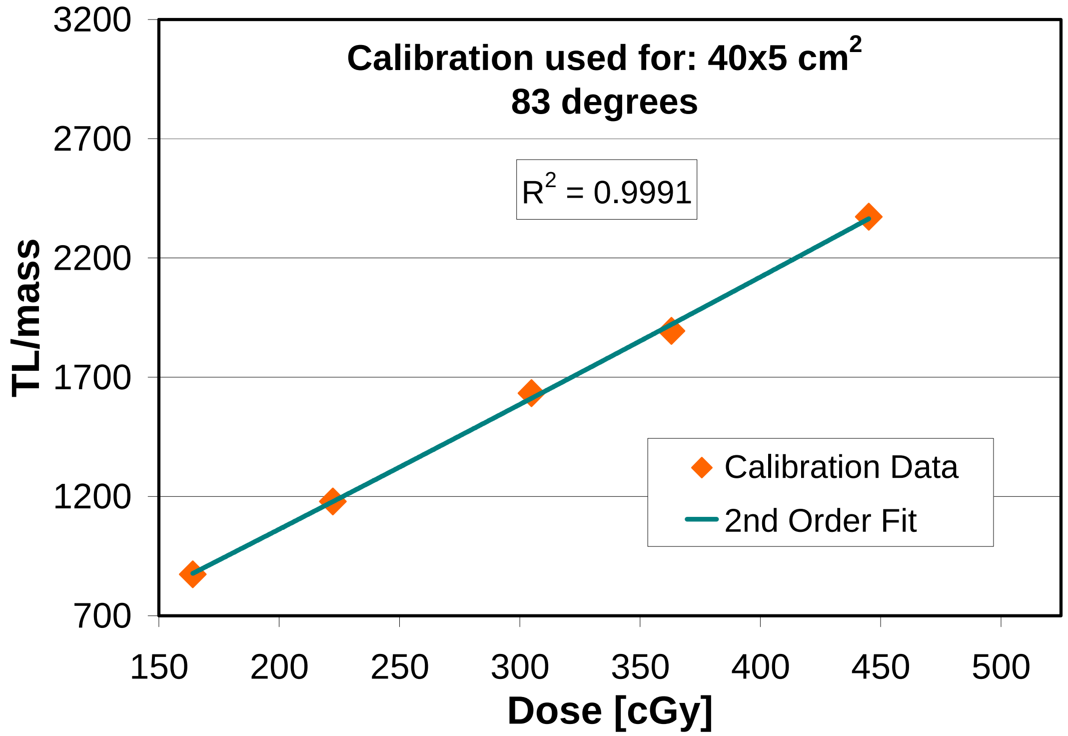

Figure 44. Calibration curve used for interpolating unknown doses measured with TLDs for the measurement of a 40x5 cm^2 beam at 83˚ angle of incidence.

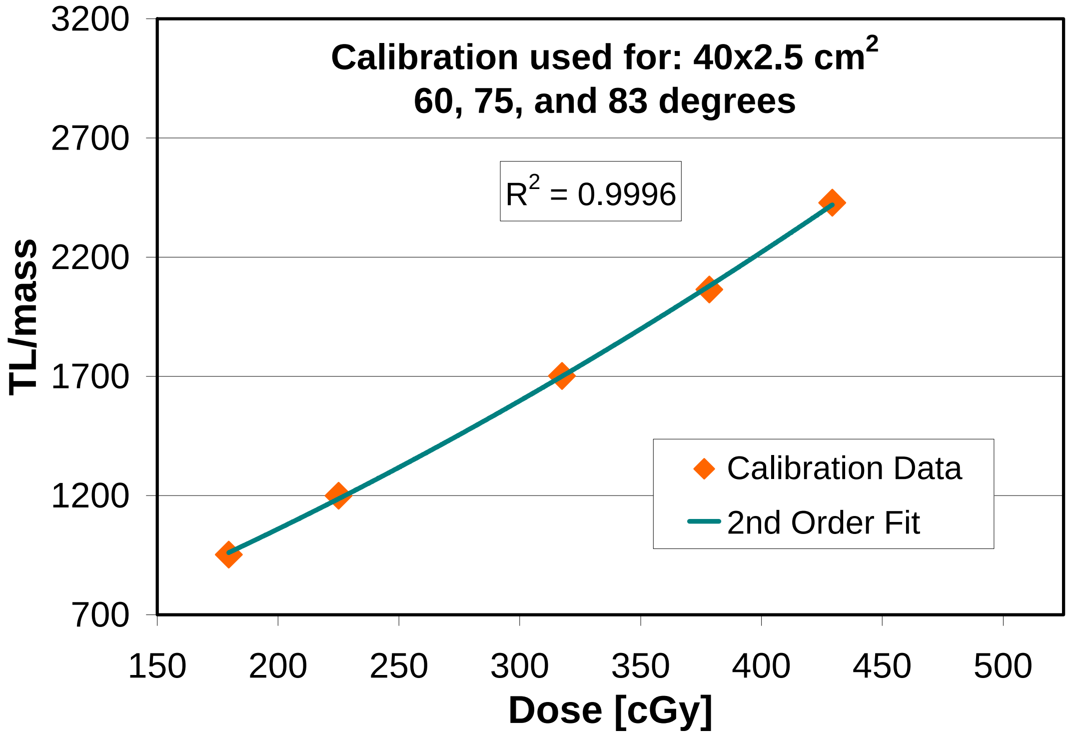

Figure 45. Calibration curve used for interpolating unknown doses measured with TLDs for the measurement of a 40x2.5 cm^2 beam at 60˚, 75˚ and 83˚ angle of incidence.

Vita

Koren Smith was born in Mamou, Louisiana, on July 27, 1982, the daughter of Ted Smith and Mary Duhon. After completing her work at Vidrine High School, in Ville Plate, Louisiana, in 2000, she entered Louisiana State University in Baton Rouge, Louisiana. She received the degree of Bachelor of Science with a major in physics in May, 2004. In August of 2004, she entered Louisiana State University's medical physics and health physics graduate program.